

Polynomial Chaos Expansions on Principal Geodesic Grassmannian Submanifolds for Surrogate Modeling and Uncertainty Quantification

Dimitris G. Giovanis^{a,c,*}, Dimitrios Loukrezis^d, Ioannis G Kevrekidis^{b,1}, Michael D. Shields^{a,c}

^a*Department of Civil & Systems Engineering, Johns Hopkins University, USA*

^b*Department of Chemical and Biomolecular Engineering, Johns Hopkins University, USA*

^c*Hopkins Extreme Materials Institute, Johns Hopkins University, USA*

^d*Institute for Accelerator Science and Electromagnetic Fields, Technische Universität Darmstadt, Germany*

Abstract

In this work we introduce a manifold learning-based surrogate modeling framework for uncertainty quantification in high-dimensional stochastic systems. Our first goal is to perform data mining on the available simulation data to identify a set of low-dimensional (latent) descriptors that efficiently parameterize the response of the high-dimensional computational model. To this end, we employ Principal Geodesic Analysis on the Grassmann manifold of the response to identify a set of disjoint principal geodesic submanifolds, of possibly different dimension, that captures the variation in the data. Since operations on the Grassmann require the data to be concentrated, we propose an adaptive algorithm based on Riemannian K-means and the minimization of the sample Fréchet variance on the Grassmann manifold to identify “local” principal geodesic submanifolds that represent different system behavior across the parameter space. Polynomial chaos expansion is then used to construct a mapping between the random input parameters and the projection of the response on these local principal geodesic submanifolds. The method is demonstrated on four test cases, a toy-example that involves points on a hypersphere, a Lotka-Volterra dynamical system, a continuous-flow stirred-tank chemical reactor system, and a two-dimensional Rayleigh-Bénard convection

*Corresponding author.

Email addresses: dgiovan1@jhu.edu (Dimitris G. Giovanis), dimitrios.loukrezis@tu-darmstadt.de (Dimitrios Loukrezis), yannisk@jhu.edu (Ioannis G Kevrekidis), michael.shields@jhu.edu (Michael D. Shields)

problem.

Keywords: Surrogate modeling, Manifold learning, Grassmannian, Principal geodesic analysis, Uncertainty quantification, Fréchet variance, Polynomial chaos expansions

1. Introduction

Computer simulations play a vital role in the field of scientific computing and its engineering applications. The principle of the simulation is to numerically solve a set of mathematical equations (e.g., nonlinear ordinary or partial differential equations) that describe the behavior of the real physical and/or engineering system (e.g., materials, climate systems, and civil infrastructure), often on a complex spatio-temporal domain. In real-world applications, such systems are complex and multiscale (and/or multiphysics), requiring very high-fidelity models to accurately capture their response. Despite the aggregation of computational power into supercomputers and the development of sophisticated algorithms to solve massive-scale problems, running a single simulation of a very high-dimensional model can be cumbersome, even with exascale computing. On top of that, since the model is an approximation of the true physics (typically based on the modeler’s knowledge and experience) with parameters calibrated to existing data and may have components (such as initial conditions or excitation) that are inherently stochastic, these systems can be highly uncertain. To increase our confidence in the predictions of the model, we need to propagate these uncertainties through the system and understand their influence on the response quantities of interest (QoIs). To this end, uncertainty quantification (UQ) provides a framework for the mathematical treatment of uncertainty in computational models [1]. However, a major limitation in performing UQ with high-fidelity models is the numerous repeated simulations of the computational model required for Monte Carlo-based methods [2, 3]. Therefore, there is a continuous effort to overcome these computational obstacles.

To reduce computational effort, it is common to employ a surrogate model (aka response surface, metamodel, or emulator) [4, 5], which is a fast-running alternative mathematical function that maps model inputs to outputs (e.g., via supervised learning), to propagate uncertainty at a significantly reduced computational cost. To construct a surrogate that can

approximate the response of a system at new points in the input parameter space, a finite number of high-fidelity model evaluations are required to provide input-output training data. The construction of accurate surrogates typically requires smooth input-output functional relations that predict low-dimensional QoIs, especially when the available training data are scarce, e.g., due to a limited simulation budget. However, these assumptions may not be realistic in real-world applications, as many systems exhibit strongly nonlinear behavior and produce high-dimensional responses for which scalar (or low-dimensional) descriptors are inadequate.

Over the last 20+ years, various surrogate modeling techniques have been proposed to accelerate UQ tasks in computational models, such as polynomial chaos expansions (PCEs) [6–8], support vector machines (SVMs) [9, 10], Gaussian processes (GPs) [11, 12], and artificial neural networks [13, 14]. Among them, the non-intrusive, regression-based PCE is an attractive choice when only limited data are available [15–17]. The PCE learns the input-output relationship in terms of a polynomial expansion, the basis polynomials of which are orthonormal with respect to the probability density function that characterizes the input variables. One of the main advantages of PCE methods is that UQ tasks such as moment estimation [18] and sensitivity analysis [19, 20] can be performed by simply post-processing the PCE coefficients. Furthermore, recent advances have enabled physical constraints to be placed on PCE models [21, 22], thus making PCE surrogates even more attractive for UQ on physics-based models.

A major challenge in UQ is the *curse of dimensionality*. For example, fast growing polynomial bases due to high-dimensional inputs pose a major obstacle to constructing PCE surrogates. To overcome this limitation, numerous sparse and/or basis-adaptive PCE methods have been proposed in the literature [23, 24]. The curse of dimensionality also arises for models with high-dimensional outputs, for example, in the form of time series or spatial fields quantities. This is the case of interest in this work.

One way to mitigate the curse of dimensionality in high-dimensional models is to use dimension reduction. Dimension reduction is an unsupervised learning task that refers to the

process of identifying and extracting *important* latent features (attributes) while preserving most of the information contained in the original dataset [25]. To identify the essential features, a variety of linear and nonlinear dimension reduction techniques can be used to map data onto lower-dimensional manifolds (aka embeddings or latent spaces). Linear dimension reduction methods such as the widely-used principal component analysis (PCA) (and the closely related singular value decomposition, SVD, and proper orthogonal decomposition, POD) apply a linear operation to the high-dimensional data to map it onto a new rotated and/or stretched basis in Euclidean space that has a lower dimension. Nonlinear dimension reduction methods, also known as manifold learning methods, assume that high-dimensional data reside on some low-dimensional nonlinear manifold. These include methods such as diffusion maps (DMaps) [26, 27], Laplacian eigenmaps [28], and Isomap [29]. For UQ purposes, surrogate model training for high-dimensional physics-based models can become tractable when dimension reduction methods are applied to high-dimensional model outputs, e.g., due to smooth functional relations between inputs and reduced outputs. As a result, dimension reduction methods are now being fully integrated into surrogate-based UQ efforts for high-dimensional models. For example, recent works of the authors have considered the construction of surrogate models using nonlinear manifold learning on the Grassmannian [30–32]. Another class of methods leverages DMaps to either draw samples from a distribution on the diffusion manifold [33–35] or construct surrogate models on the diffusion manifold [36–38]. Lataniotis et al. [39] coupled kernel PCA with Kriging and PCE to extend surrogates to high-dimensional models. Recently, a systematic survey of 14 different manifold learning methods was undertaken for high-dimensional surrogate modeling by Kontolati et al. [40], who devised the manifold PCE (m-PCE).

An alternative means of constructing surrogates for high dimensional models uses deep learning. Recent advances have allowed the identification of latent representations of data using multi-layer perceptrons, autoencoders [41], and convolutional neural networks [42] for building surrogate models with low-dimensional input and output parameters [13, 14, 43–46]. Although deep learning-based surrogates are capable of capturing complex nonlinear

relations between high-dimensional inputs and outputs, they are very costly to train, rely on the heuristic choice of the network architecture and the calibration of a huge number of hyperparameters. Very recently, the class of neural operators – specifically the Deep Operator Network (DeepONet) [47] and Fourier Neural Operator (FNO) [48] and their variants – have become very attractive options to build continuous machine learned surrogate solution operators. These operators have been systematically compared (under certain conditions [49]) with the general class of manifold learning-based finite dimensional regressors (since we do not learn solution operators) of the type we study here (specifically the manifold PCE, m-PCE [40]) to compare model generalization and robustness to noise [49]. Another particularly noteworthy candidate for surrogate model construction in UQ are the general class of physics informed neural networks (PINNs) [50] and in particular their extension for physics informed neural operators [51]. A detailed discussion of these methods is out of the scope of this work though.

In this work we introduce a novel framework based on Principal Geodesic Analysis (PGA) on the Grassmann manifold, which combines manifold learning principles with PCE surrogate model construction for the prediction of dimension-reduced solutions that can be used to reconstruct approximate full model solutions from on a limited number of model evaluations. We are particularly interested in complex models that generate high-dimensional outputs (e.g., time series or spatial field quantities) that may be computationally expensive to run. Similar to our previous works [30, 31, 52], each data point corresponds to a vector of the full-field solution. The projection onto the Grassmann manifold is performed by recasting the solution vector into a matrix and then via singular value decomposition (SVD) the representative on the Grassmann manifold is obtained. The reader is referred to [31] for a detailed discussion on the motivation that underpins such representation.

The remainder of the paper is organized as follows. Theoretical concepts of the Grassmann manifold and PGA are briefly introduced in Section 2. We also present the important ingredients of the proposed clustering framework of points on the Grassmann manifold which is based on the minimization of the Fréchet variance. This step is necessary for developing local

surrogate models. Section three discuss in detail the steps required for (i) performing local geodesic submanifold interpolation using polynomial chaos expansion within each submanifold and, (ii) obtaining the full solutions from the reduced-order predictions. The performance of the proposed approach is assessed by three illustrative applications given in Section 4. The first application involves a toy-example that involves data on the sphere. In the second application, the method is applied to predict time-evolution on the classic Lotka-Volterra (predator-prey) dynamical system. The third application deals with a continuous stirred-tank reactor system. The fourth example involves predicting Rayleigh-Bénard convection in a two-dimensional rectangular domain. Finally, Section 5 presents the conclusions.

The distinct components of the proposed method have been implemented¹ using UQpy (Uncertainty Quantification with python [53, 54]), a general-purpose open-source software for modeling uncertainty in physical and mathematical systems, and Geomstats [55, 56].

2. Principal Geodesic Analysis on the Grassmann Manifold

In this section, we briefly review the geometry of the Grassmann manifold and the basic concepts of Principal Geodesic analysis (PGA).

2.1. Grassmann manifold

The Grassmann manifold $\mathcal{G}(p, n)$ is a (smooth, compact) matrix manifold defined as the set of all p -dimensional linear subspaces in \mathbb{R}^n . The Grassmann manifold can be viewed as a quotient manifold of the Stiefel manifold $\mathcal{St}(p, n)$ [57], which is the manifold of all p -dimensional orthonormal matrices in \mathbb{R}^n . In this setting, a matrix $\mathbf{U} \in \mathcal{St}(p, n)$ can be considered representative of subspace $\mathcal{U} \in \mathcal{G}_{p,n}$ if its columns span the corresponding subspace, i.e., $\mathcal{U} \equiv \text{span}(\mathbf{U})$. Therefore, the Stiefel representation of the Grassmannian provides a natural and intuitive representation for subspace analysis [58, 59]. We specifically aim to use a subspace representation of a system due to the difficulty in assessing similarity between high-dimensional data, i.e., data generated by models with high-dimensional QoIs.

¹The code to reproduce the results for all numerical examples will be available in <https://github.com/dgiovanis> after the publication of the paper.

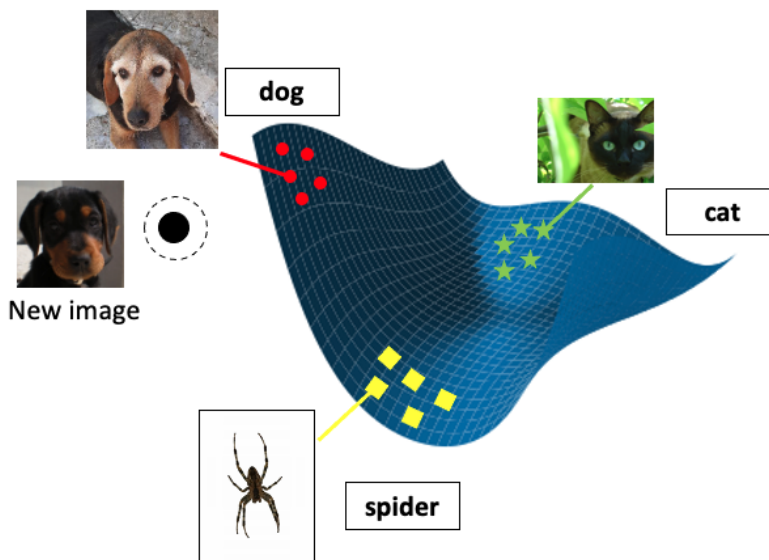


Figure 1: For a set of training images that correspond to three different classes, namely cats, dogs, and spiders, we can classify these images based on their respective subspaces on the Grassmannian and when a new image (e.g., an image of a dog) is introduced we can assign it to the appropriate class.

The Grassmann manifold is an important mathematical modeling construct for several applications, ranging from problems in machine learning [60] and computer vision and image processing (see e.g. Figure 1) [61], to low-rank matrix optimization problems [62], dynamic low-rank decomposition [63] and model reduction [27, 30, 31, 64, 65].

On the Grassmann, the curve with the minimum length between two points $\mathbf{U}_1, \mathbf{U}_2$ is called the geodesic path and it can be parameterized by a function: $\gamma : t \in [0, 1] \rightarrow \mathcal{G}_{p,n}$, where $\gamma(0) = \mathbf{U}_1$ and $\gamma(1) = \mathbf{U}_2$ are the initial conditions. The geodesic is determined by solving a second-order differential equation on $\mathcal{G}_{p,n}$ that corresponds to motion along the curve with constant tangential velocity (i.e., all acceleration is normal to the manifold). The length of the geodesic path is called the geodesic distance and is defined by a nonlinear function of the principal angles between subspaces, $\theta_i = \cos^{-1} \Sigma_i$ calculated from the full SVD given by $\mathbf{U}_1^T \mathbf{U}_2 = \mathbf{\Phi} \mathbf{\Sigma} \mathbf{\Psi}^T$. Several such distance measures on the Grassmann manifold have been proposed in the literature [66]. Regardless of the distance measure, the notion of similarity is maximized when the distance between two subspaces is zero. An issue that

often arises in computing distances between subspaces representing physical models is that the subspaces may have different dimensions [31]. In such cases, the infinite $\mathcal{G}_{\infty,n}$ and the doubly infinite $\mathcal{G}_{\infty,\infty}$ Grassmannian distances proposed by Ye and Lim [67] can be used. For a detailed discussion on handling different Grassmann dimensions for surrogate construction the reader is referred to [31].

The tangent space $\mathcal{T}_{\mathbf{U}_1}$ of the Grassmannian with origin at \mathbf{U}_1 is a flat inner-product space composed of subspaces on the plane tangential to $\mathcal{G}_{p,n}$ at \mathbf{U}_1 . In the neighborhood of \mathbf{U}_1 , a point \mathbf{U}_2 can be mapped onto the tangent plan $\mathcal{T}_{\mathbf{U}_1}$ using the logarithmic mapping $\log_{\mathbf{U}_1}(\mathbf{U}_2) = \mathbf{\Gamma}$, while the inverse mapping from the tangent space to the manifold can be performed with the associated exponential map $\exp_{\mathbf{U}_1}(\mathbf{\Gamma}) = \mathbf{U}_2$. An analytical formulation of the mappings is presented in Appendix A. Points on the manifold can be mapped to a reproducing kernel Hilbert space by using appropriate kernels $\mathcal{K} : \mathcal{G}_{p,n} \times \mathcal{G}_{p,n} \rightarrow \mathbb{R}$, where \mathcal{K} is positive semi-definite and invariant to the choice of basis. Several families of Grassmannian kernels exist in the literature [68].

Given a distance function $d(\cdot, \cdot)$ and a set of \mathcal{N} points on $\mathcal{G}_{p,n}$, the sample Karcher mean ($\hat{\boldsymbol{\mu}}$) and the sample Fréchet variance (σ^2) can be defined as [69]:

$$\hat{\boldsymbol{\mu}} = \arg \min_{\omega \in \mathcal{G}_{p,n}} \frac{1}{\mathcal{N}} \sum_{i=1}^{\mathcal{N}} d^2(\mathbf{U}_i, \omega) \in \mathbb{R}^{n \times p} \quad (1)$$

and

$$\sigma^2 = \frac{1}{\mathcal{N}} \sum_{i=1}^{\mathcal{N}} d^2(\mathbf{U}_i, \hat{\boldsymbol{\mu}}) \in \mathbb{R}, \quad (2)$$

respectively. Various iterative algorithm such as Newton's method or the first-order gradient descent [58, 70, 71] be used in order to estimate the sample Karcher mean. However, a unique optimal solution is not always guaranteed [71, 72]. If the ensemble of Grassmann points has a radius greater than $\pi/4$, then the exponential and logarithmic maps are no longer bijective, and the Karcher mean is no longer unique [71].

2.2. Principal Geodesic Analysis (PGA)

In Euclidean space, Principal Component Analysis (PCA) is arguably the leading linear method for identifying a low-dimensional subspace that best represents the variability of the data [73]. However, PCA cannot be directly applied to data on the Grassmann manifold due to its nonlinear structure. PGA generalizes the PCA concept to data on manifolds by seeking a sequence of nested geodesic submanifolds that maximizes the sample Fréchet variance of the projected data[74].

Before introducing PGA, let us briefly recall the basic concepts of PCA in Euclidean space. Consider the vector $\mathbf{X} = [\mathbf{x}_1, \mathbf{x}_2, \dots, \mathbf{x}_N]^\top$ of \mathcal{N} (zero-mean) points $\mathbf{x}_i \in \mathbb{R}^d$. PCA seeks the orthonormal basis $[\mathbf{v}_1, \mathbf{v}_2, \dots, \mathbf{v}_k] \in \mathbb{R}^k$ such that the basis vectors, \mathbf{v}_i , define linear subspaces that align with the principal directions of the variance. That is, \mathbf{v}_1 aligns with the direction of maximum variance, \mathbf{v}_2 aligns with the direction of second highest variance, and so on. The basis can be computed as the set of ordered eigenvectors of the sample covariance matrix of the data through a recursive relationship or through SVD of the matrix $\mathbf{X}^T \mathbf{X}$.

PGA generalizes PCA by first extending the notion of a linear subspace. For general manifolds, the generalization of a linear subspace is referred to as a *geodesic submanifold*. Recall that a geodesic is a curve with the shortest length between points on the manifold; hence it is the generalization of a straight line. It is therefore natural to represent one-dimensional subspaces on a manifold, \mathcal{M} , using geodesics. A submanifold, \mathcal{H} , is called geodesic if all geodesics of \mathcal{H} passing through x are also geodesics of the manifold \mathcal{M} . However, the geodesics of a submanifold \mathcal{H} of a manifold \mathcal{M} are not necessarily geodesics of \mathcal{M} itself. For example, the sphere \mathcal{S}^2 is a submanifold of \mathbb{R}^3 , but its geodesics are great circles, which are not geodesics of \mathbb{R}^3 – whose geodesics are straight lines. Importantly, geodesic submanifolds defined at a point \mathbf{x} preserve distances to \mathbf{x} .

PGA then defines the “principal directions” by identifying the geodesic submanifolds that best represent the Fréchet variance – referred to as *principal geodesic submanifolds*. Because geodesic submanifolds preserve the distance to a point \mathbf{x} and the Fréchet variance is defined in terms of a mean square distance to the Karcher mean, the principal geodesic submanifolds

defined at the Karcher mean are a natural generalization of the principal linear subspaces in PCA.

The projection of a point $\mathbf{U}_i \in \mathcal{G}_{p,n}$ onto a geodesic submanifold \mathcal{H} is defined as the point $y \in \mathcal{H}$ that is nearest to \mathbf{U}_i in Riemannian distance:

$$\pi_{\mathcal{H}}(\mathbf{U}_i) = \arg \min_{y \in \mathcal{H}} d^2(\mathbf{U}_i, y). \quad (3)$$

However, existence and uniqueness of the point y is only guaranteed by restricting the optimization to a small enough neighborhood around the mean. Projection of the point \mathbf{U}_i onto a geodesic submanifold can be approximated linearly in the tangent space $\mathcal{T}_{\hat{\mu}}$ of $\mathcal{G}_{p,n}$. Let $\mathcal{H} \subset \mathcal{G}_{p,n}$ be a geodesic submanifold at a point $\omega \in \mathcal{G}_{p,n}$, then the projection \mathbf{U}_i is approximated by

$$\pi_{\mathcal{H}}(\mathbf{U}_i) = \arg \min_{y \in \mathcal{H}} \|\text{Log}_{\mathbf{U}_i}(y)\|^2 \approx \arg \min_{\mathbf{y} \in \mathcal{H}} \|\text{Log}_{\omega}(\mathbf{U}_i) - \text{Log}_{\omega}(\mathbf{y})\|^2 \quad (4)$$

where $\text{Log}_{\omega}(\mathbf{y})$ is simply a vector in $\mathcal{T}_{\omega}\mathcal{H}$. We can rewrite Eq. (4) in terms of tangent vectors as

$$\text{Log}_{\omega}(\pi_{\mathcal{H}}(\mathbf{U}_i)) \approx \arg \min_{\mathbf{v} \in \mathcal{T}_{\omega}\mathcal{H}} \|\text{Log}_{\omega}(\mathbf{U}_i) - \mathbf{v}\|^2 \quad (5)$$

where $\text{Log}_{\omega}(\pi_{\mathcal{H}}(\mathbf{U}_i))$ implies that the projection operation in the tangent space, transforming the minimization on the manifold into one in the linear subspace $\mathcal{T}_{\omega}\mathcal{H}$. Therefore, if $\mathbf{v} = [\mathbf{v}_1, \mathbf{v}_2, \dots, \mathbf{v}_k]^{\top}$ is an orthonormal basis for $\mathcal{T}_{\omega}\mathcal{H}$, the projection operator can be approximated by

$$\text{Log}_{\omega}(\pi_{\mathcal{H}}(\mathbf{U}_i)) \approx \sum_{i=1}^k \langle \mathbf{v}_i, \text{Log}_{\omega}(\mathbf{U}_i) \rangle \quad (6)$$

In the same way that PCA seeks to find the set of linear subspaces that maximize the projected variance, PGA aims to identify the set of nested geodesic submanifolds that maximize the projected Fréchet variance of the data, i.e. the principal geodesic submanifolds. To define principal geodesic submanifolds from a set of points on the Grassmann manifold, we construct an orthonormal basis of vectors $\mathbf{v}_1, \mathbf{v}_2, \dots, \mathbf{v}_k$ spanning the tangent space

$\mathcal{T}_{\hat{\boldsymbol{\mu}}}$ defined at the Karcher mean $\hat{\boldsymbol{\mu}}$. These vectors form a sequence of nested subspaces $V_k = \text{span}(\mathbf{v}_1, \mathbf{v}_2, \dots, \mathbf{v}_k) \cap U$, where $U \subset \mathcal{T}_{\hat{\boldsymbol{\mu}}}$ is a neighborhood around $\hat{\boldsymbol{\mu}}$ in which the projection operation is well defined for all geodesic submanifolds of $\text{Exp}_{\hat{\boldsymbol{\mu}}}(U)$. The principal geodesic submanifolds are the images of V_k under the exponential map $\mathcal{H}_k = \text{Exp}_{\hat{\boldsymbol{\mu}}}(V_k)$. We start by defining the first principal direction to maximize the projected Fréchet variance along the corresponding geodesic:

$$v_1 = \arg \max_{\|v\|=1} \sum_{i=1}^{\mathcal{N}} \|\log_{\hat{\boldsymbol{\mu}}}(\pi_{\mathcal{H}_1}(\mathbf{U}_i))\|^2 \quad (7)$$

where $\mathcal{H}_1 = \text{Exp}_{\hat{\boldsymbol{\mu}}}(\text{span}(\{v\} \cap U))$. The remaining principal directions are defined recursively as

$$v_k = \arg \max_{\|v\|=1} \sum_{i=1}^{\mathcal{N}} \|\log_{\hat{\boldsymbol{\mu}}}(\pi_{\mathcal{H}_k}(\mathbf{U}_i))\|^2 \quad (8)$$

where $\mathcal{H}_k = \text{Exp}_{\hat{\boldsymbol{\mu}}}(\text{span}(\{v_1, \dots, v_{k-1}, v\} \cap U))$.

Practically speaking, PGA is performed by simply applying standard PCA in the tangent space $\mathcal{T}_{\hat{\boldsymbol{\mu}}}$. The algorithm for PGA on the Grassmann manifold is given in Algorithm 1.

Algorithm 1 Principal Geodesic Analysis on the Grassmann

Require: Points $\mathbf{U}_1, \mathbf{U}_2, \dots, \mathbf{U}_{\mathcal{N}} \in \mathcal{G}_{p,n}$

Calculate $\hat{\boldsymbol{\mu}} = \arg \min_{\omega \in \mathcal{G}_{p,n}} \frac{1}{\mathcal{N}} \sum_{i=1}^{\mathcal{N}} d^2(\mathbf{U}_i, \omega)$ ▷ Karcher mean

Find $\mathbf{u}_i = \log_{\hat{\boldsymbol{\mu}}}(\mathbf{U}_i)$ ▷ Projection on the tangent space $\mathcal{T}_{\hat{\boldsymbol{\mu}}}$

$\mathbf{S} = \frac{1}{\mathcal{N}} \sum_{i=1}^{\mathcal{N}} \mathbf{u}_i \mathbf{u}_i^\top$ ▷ Covariance matrix of tangent vectors

$\text{Eig}(\mathbf{S}) \rightarrow \{\mathbf{v}_k, \lambda_k\}$ ▷ Eigenvectors and eigenvalues of \mathbf{S}

3. Dimension reduction on the Grassmann based using local PGAs

Consider a model $\mathcal{M}(\boldsymbol{\theta})$ (e.g., a stochastic partial differential equation) where $\boldsymbol{\theta} \in \mathbb{R}^d$ is a random vector having joint probability distribution function (PDF) $\varrho_{\boldsymbol{\theta}}(\boldsymbol{\theta})$ defined on the probability space $(\Omega, \Sigma, \mathbb{P})$, where Ω is the sample space, Σ the set of events, and \mathbb{P} the probability measure. Given an experimental design $\Theta = \{\boldsymbol{\theta}_1, \boldsymbol{\theta}_2, \dots, \boldsymbol{\theta}_{\mathcal{N}}\}$, let us denote the corresponding full-field solutions (responses) as $\mathbf{y}_i = \mathcal{M}(\boldsymbol{\theta}_i) \in \mathbb{R}^n$, which are assumed to

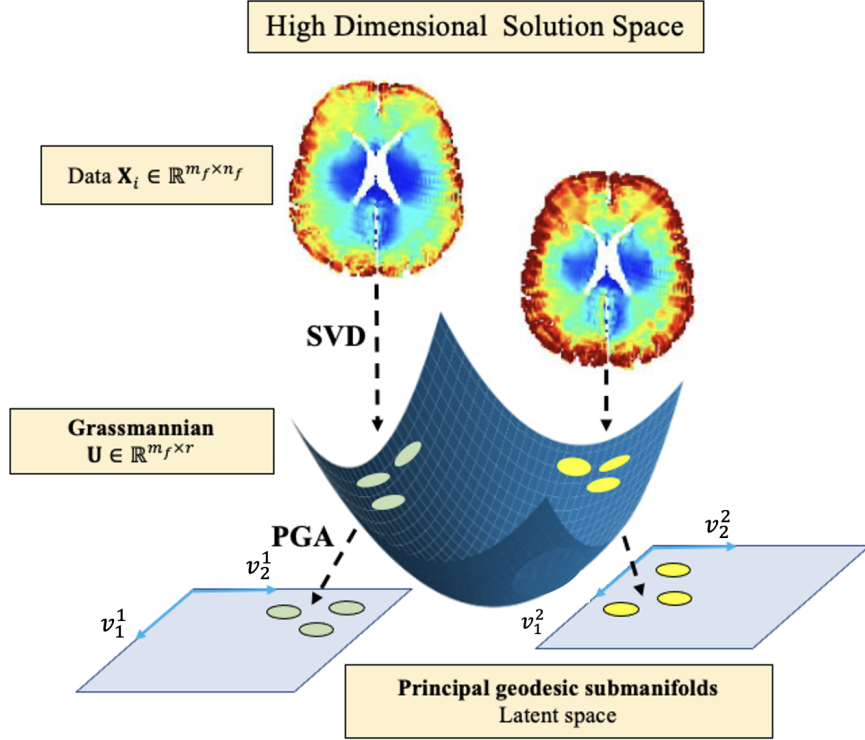


Figure 2: Illustration of the proposed two-phase dimension reduction scheme using Grassmann manifold projection and principal geodesic analysis. The strain field images of computational head models are adopted from [65]. Each circle on the manifold corresponds to a realization of the strain field. Distinct colors represent different clusters on the Grassmann.

have very high dimensionality, e.g., $n \sim \mathcal{O}(10^{4-6})$. We first aim to reduce the dimension of each response \mathbf{y}_i in such a way that its salient information, such as the intrinsic geometry of the solution space, is retained. Note that for most real-world applications, the size of the experimental design is usually small to medium, e.g., $\mathcal{N} \sim \mathcal{O}(10^{1-3})$.

The proposed dimension reduction method is performed in two stages: First, each response \mathbf{y}_i is projected onto a Grassmann manifold using thin SVD [27, 30, 38, 75]. In the second stage, we perform unsupervised learning on the Grassmann using an extension of K-means for clustering on the manifold [76]. Since the optimal data partition (number of clusters) is not known *a priori*, we propose a method to identify the minimum necessary number of clusters automatically through minimization of the sample Fréchet variance. Then, for each cluster, we perform PGA to further reduce the dimension of the data. An illustration of

the proposed two-stage dimension reduction method is shown in Figure 2, while a detailed description follows.

3.1. Projection on the Grassmann manifold

To exploit the subspace structure of the high-dimensional model response, we first project each response $\mathbf{y}_i \in \mathbb{R}^{n(=m_f \times n_f)}$ onto the Grassmannian by means of thin-SVD, such that $\mathbf{y}_i = \mathbf{U}_i \mathbf{\Sigma}_i \mathbf{V}_i^T$, where $\mathbf{U}_i \in \mathbb{R}^{m_f \times p_i}$ and $\mathbf{V}_i \in \mathbb{R}^{n_f \times p_i}$ are orthonormal matrices, i.e., $\mathbf{U}_i^T \mathbf{U}_i = \mathbf{I}_{p_i}$, $\mathbf{V}_i \mathbf{V}_i^T = \mathbf{I}_{p_i}$, and $\mathbf{\Sigma}_i \in \mathbb{R}^{p_i \times p_i}$ is a diagonal matrix whose non-zero elements are the singular values ordered by magnitude. Note that p_i is the rank of \mathbf{y}_i , which is determined during the SVD based on a prescribed tolerance. By performing SVD, each response is now represented by two matrices i.e., points on two Grassmann manifolds, and a vector i.e., a point in Euclidean space. In general, two responses \mathbf{y}_i and \mathbf{y}_j might have different ranks ($p_i \neq p_j$), thus also a different number of columns. This means that \mathbf{U}_i and \mathbf{U}_j lie on different Grassmann manifolds, i.e., $\mathbf{U}_i \in \mathcal{G}_{p_i, m_f}$ and $\mathbf{U}_j \in \mathcal{G}_{p_j, m_f}$. In this case, we can embed the points into the infinite Grassmannian $\mathcal{G}_{\infty, m_f} \equiv \mathcal{G}_{p_{\infty}, m_f}$, with $p_{\infty} = \max(p_1, p_2, \dots)$, and perform the calculations there.

3.2. Unsupervised learning on the Grassmann

Given a set of points on the Grassmann manifold, we next perform a modified K-means clustering [77]. For a prescribed number of clusters, n_c , K-means partitions data (x_1, x_2, \dots, x_N) by minimizing the objective function:

$$J = \sum_{j=1}^N \sum_{k=1}^{n_c} r_{jk} \|x_j - \mu_k\|^2 \quad (9)$$

where μ_k are the centroids, and r_{jk} is equal to 1 if $x_j \in S_k$ and 0 otherwise, where $S_k = \{x_j : \|x_j - \mu_k\|^2 \leq \|x_j - \mu_m\|^2, \forall m \neq k\}$. The algorithm starts by randomly choosing n_c points from the data set to serve as initial guesses of the cluster centroids. The distance from each data point to each centroid is computed, and the data is assigned to its closest centroid. The centroid then is replaced by the mean of the partitioned data and the steps are repeated until all n_c centroids are identified.

K-means is effective for data in Euclidean space where the notion of similarity is defined through the Euclidean distance. However, when the data have intrinsic geometric features constrained on some manifold, K-means performed in Euclidean space may fail to capture similarity. A variant of K-means for data that lie on Riemannian manifolds (such as the Grassmannian) was introduced in [76]. In this variation, the objective function to minimize takes the form:

$$J = \sum_{j=1}^{\mathcal{N}} \sum_{k=1}^{n_c} r_{jk} d_{\mathcal{G}}(\mathbf{U}_j, \boldsymbol{\mu}_k)^2 \quad (10)$$

where $d_{\mathcal{G}}(\cdot)$ is the Riemannian distance (i.e. Grassmann distance) and r_{jk} is equal to 1 if $\mathbf{U}_j \in S_k$ and 0 otherwise, where $S_k = \{\mathbf{U}_j : d_{\mathcal{G}}(\mathbf{U}_j, \boldsymbol{\mu}_k)^2 \leq d_{\mathcal{G}}(\mathbf{U}_j, \boldsymbol{\mu}_m)^2, \forall m \neq k\}$. Again, the algorithm starts by randomly selecting n_c points from the data as the centroids $\boldsymbol{\mu}_k$ and computing the Riemannian distance (using the logarithmic map) between each point \mathbf{U}_j , and the centroids. Then, each point is assigned to its closest centroid which is then replaced by the Karcher mean of the partitioned data (computed by the stochastic gradient descent method [71]). The process is repeated until all n_c centroids are identified.

K-means requires the number of clusters, n_c , to be specified a priori. However, this number is not known beforehand for arbitrary models where variations in performance are not already known. We propose a novel iterative algorithm to identify the optimal number of clusters for points on the Grassmann that begins with a small number of clusters, i.e., $n_c = 2$. At each iteration (*iter*) we increase the number of clusters by one, partition the data using Riemannian K-means, and compute the Karcher mean $\boldsymbol{\mu}_c$ and the sample Fréchet variance σ_i^2 for each cluster. Next, we compute the sample Fréchet variance of all Karcher means $\boldsymbol{\sigma}_{\boldsymbol{\mu}}^2$ and we compute the following score:

$$\lambda_{S_h}^{n_c} = \frac{\boldsymbol{\sigma}_{\boldsymbol{\mu}}^2}{\sum_{i=2}^{n_c} \sigma_i^2}. \quad (11)$$

which quantifies the goodness of the clustering. The definition of this coefficient is similar to the definition of the silhouette Coefficient used to validate the clustering when dealing with data in Euclidean spaces. We repeat this process until the number of points N_h in at

Algorithm 2 Optimization based on Riemannian K-means on the Grassmann

Require: minimum number of points in a cluster $N_h \geq 5$

```

 $iter = 1$  ▷ iterations number
 $\lambda_{S_h}[0] = 0$ 
 $l = 2$  ▷ total number of clusters
 $n_c = 2$  ▷ minimum number of clusters
 $\bar{f}_{iter} = \infty$ 
while  $\min(N_1, \dots, N_{n_c}) \leq 5$  do
  Perform Riemannian K-means with  $n_c$  clusters
  for  $h = 1 : n_c$  do
     $\sigma_h^2 = 1/N_h \sum_{i=1}^{N_h} d_{\mathcal{G}}^2(\mathbf{U}_i, \hat{\boldsymbol{\mu}}_{\mathbf{U},h})$  ▷ Compute the sample Fréchet variance
  end for
   $\lambda_{S_h} = \frac{1}{n_c} \sum_{c=2}^{n_c} \lambda_{S_h}^{(c)}$  ▷ Silhouette coefficient
   $iter = iter + 1$  ▷ next iteration
   $n_c = n_c + 1$  ▷ increase number of clusters by one
end while
  Perform Riemannian K-means with  $n_c$  clusters

```

least one of the clusters is less or equal to a minimum value, e.g., $N_h \leq 5$. The optimal number of clusters corresponds to the largest value of the silhouette coefficient $\lambda_{S_h}^{n_c}$.

3.3. Local PGA on the Grassmann

Once the optimal number of clusters K has been identified and the data on the manifold have been appropriately partitioned into clusters C_h , $h = 1, \dots, n_c$, a second dimension reduction is performed using PGA on each cluster. The goal is to embed the points in latent geodesic submanifolds that best describes the geometric variability of the data on the manifold. PGA is performed in three steps, for each cluster C_i [74]: (1) lift the points from the manifold to a well-defined tangent space using the logarithmic map; (2) perform PCA in the tangent space; (3) map the results back to the manifold by an exponential map. These steps are presented in detail next.

Step 1: Project points $\{\mathbf{U}_j, \mathbf{V}_j\}_{j=1}^{N_h} \in C_h$, where N_h is the total number of data in cluster h , onto the tangent spaces with origins at the corresponding Karcher means $\hat{\boldsymbol{\mu}}_{\mathbf{U},h}$ and $\hat{\boldsymbol{\mu}}_{\mathbf{V},h}$,

i.e.,

$$\{\mathbf{U}_j \in \mathcal{G}_{p_\infty, m_f}\}_{j=1}^{N_h} \xrightarrow{\text{Log}_{\hat{\mu}}} \{\mathbf{\Gamma}_j^u \in \mathcal{T}_{\hat{\mu}_{\mathbf{U},h}}\}_{j=1}^{N_h}, \quad (12a)$$

$$\{\mathbf{V}_j \in \mathcal{G}_{p_\infty, N_f}\}_{j=1}^{N_h} \xrightarrow{\text{Log}_{\hat{\mu}}} \{\mathbf{\Gamma}_j^v \in \mathcal{T}_{\hat{\mu}_{\mathbf{V},h}}\}_{j=1}^{N_h}, \quad (12b)$$

where the indices u, v of $\mathbf{\Gamma}_j$ represent actions on the left eigenvector \mathbf{U}_j and the right eigenvector \mathbf{V}_j in the tangent space, respectively (see [Appendix A](#) for details on computation of matrices $\mathbf{\Gamma}$). Ensure $\mathbf{\Gamma}_j^u \in U_u^h, \forall j$ where $U_u^h \subset \mathcal{T}_{\hat{\mu}_{\mathbf{U},h}}$ is a neighborhood such that the projection $\text{Exp}_{\hat{\mu}_{\mathbf{U},h}}(U_u^h)$ is well-defined. Similarly ensure $\mathbf{\Gamma}_j^v \in U_v^h \subset \mathcal{T}_{\hat{\mu}_{\mathbf{V},h}}$.

Step 2: For each cluster C_h , construct an orthonormal basis of tangent vectors. The first principal direction is chosen to maximize the projected variance along the corresponding geodesic, while the remaining principal directions are defined recursively.

$$\boldsymbol{\xi}_1 = \arg \max_{\|\boldsymbol{\xi}\|=1} \sum_{i=1}^{N_h} \|\log_{\hat{\mu}_{\mathbf{U},h}}(\pi_{\mathcal{H}}(\mathbf{U}_i))\|^2, \quad \mathcal{H} = \text{exp}_{\hat{\mu}_{\mathbf{U},h}}(\text{span}(\{\boldsymbol{\xi}\}) \cap U_u^h) \quad (13a)$$

$$\boldsymbol{\xi}_k = \arg \max_{\|\boldsymbol{\xi}\|=1} \sum_{i=1}^{N_h} \|\log_{\hat{\mu}_{\mathbf{U},h}}(\pi_{\mathcal{H}}(\mathbf{U}_i))\|^2, \quad \mathcal{H} = \text{exp}_{\hat{\mu}_{\mathbf{U},h}}(\text{span}(\{\boldsymbol{\xi}_1, \dots, \boldsymbol{\xi}_{d_u-1}, \boldsymbol{\xi}\}) \cap U_u^h) \quad (13b)$$

$$\boldsymbol{\phi}_1 = \arg \max_{\|\boldsymbol{\phi}\|=1} \sum_{i=1}^{N_h} \|\log_{\hat{\mu}_{\mathbf{V},h}}(\pi_{\mathcal{H}}(\mathbf{V}_i))\|^2, \quad \mathcal{H} = \text{exp}_{\hat{\mu}_{\mathbf{V},h}}(\text{span}(\{\boldsymbol{\phi}\}) \cap U_v^h) \quad (13c)$$

$$\boldsymbol{\phi}_k = \arg \max_{\|\boldsymbol{\phi}\|=1} \sum_{i=1}^{N_h} \|\log_{\hat{\mu}_{\mathbf{V},h}}(\pi_{\mathcal{H}}(\mathbf{V}_i))\|^2, \quad \mathcal{H} = \text{exp}_{\hat{\mu}_{\mathbf{V},h}}(\text{span}(\{\boldsymbol{\phi}_1, \dots, \boldsymbol{\phi}_{d_v-1}, \boldsymbol{\phi}\}) \cap U_v^h) \quad (13d)$$

In practice, this is performed by simply applying standard PCA on the tangent vectors [\[56\]](#).

Step 3: Form a sequence of nested subspaces.

$$\mathcal{U}_k^h = \text{span}(\boldsymbol{\xi}_1, \boldsymbol{\xi}_2, \dots, \boldsymbol{\xi}_{d_u}; \in \mathcal{T}_{\hat{\mu}_{\mathbf{U},h}}) \quad (14a)$$

$$\mathcal{V}_k^h = \text{span}(\boldsymbol{\phi}_1, \boldsymbol{\phi}_2, \dots, \boldsymbol{\phi}_{d_v}; \in \mathcal{T}_{\hat{\mu}_{\mathbf{V},h}}) \quad (14b)$$

where d_u and d_v are the dimensions of the corresponding subspaces. The principal geodesic

submanifolds are the images of the \mathcal{U}_k^h and \mathcal{V}_k^h under the exponential maps $\text{Exp}_{\hat{\mu}_{\mathbf{U},h}}(\mathcal{U}_k^h)$ and $\text{Exp}_{\hat{\mu}_{\mathbf{V},h}}(\mathcal{V}_k^h)$, respectively.

In general, each cluster may require a different number of principal geodesic submanifolds in order to maximize the projected variance of the data. This number will depend on variability within each cluster. Therefore, by comparing the number of principal geodesic submanifolds across the clusters, we can identify regions of the space over which sharp changes in system behavior occur.

4. Geodesic submanifold interpolation via polynomial chaos expansions

In this section, we propose a method to construct polynomial chaos surrogate models on the lower-dimensional geodesic submanifolds. First, the basic concepts of polynomial chaos expansion (PCE) are discussed. This is followed by a PCE formulation to map from the input space to the low-dimensional latent space. Finally, the exponential mapping and inverse SVD are used to reconstruct the full-field response.

4.1. Polynomial chaos expansion

PCE is one of the most widely-used surrogate modeling techniques to accelerate UQ tasks in computational physics-based modeling [78–80]. PCE approximates the response of the model $\mathcal{M}(\boldsymbol{\theta})$ by an expansion of multi-dimensional polynomials that are orthogonal with respect to the PDF of the input random variables $\boldsymbol{\theta}$. By the Doob-Dynkin lemma [81], the response of the model is also a random variable parametrized by $\boldsymbol{\theta}$. Note that in our case we consider a vector-valued response, i.e., $\mathcal{M}(\boldsymbol{\theta}) \equiv \mathbf{y} \in \mathbb{R}^n$.

Provided that the quantity $\mathbb{E}[\|\mathbf{y}\|^2]$ (where $\|\cdot\|$ is the Euclidean norm) is finite, PCE is a spectral approximation of the form

$$\mathcal{M}(\boldsymbol{\theta}) \approx \widetilde{\mathcal{M}}(\boldsymbol{\theta}) = \sum_{\boldsymbol{\alpha} \in \mathbb{N}^d} \mathbf{a}_{\boldsymbol{\alpha}} \Psi_{\boldsymbol{\alpha}}(\boldsymbol{\theta}), \quad (15)$$

where the coefficients $\mathbf{a}_{\boldsymbol{\alpha}} = [a_{\boldsymbol{\alpha}}^{(1)}, \dots, a_{\boldsymbol{\alpha}}^{(n)}]^\top$ are deterministic vectors and $\Psi_{\boldsymbol{\alpha}}$ are multivariate polynomials that are orthonormal with respect to the joint PDF $\varrho_{\boldsymbol{\theta}}$, such that $\mathbb{E}[\Psi_{\boldsymbol{\alpha}} \Psi_{\boldsymbol{\beta}}] = 1$

if $\boldsymbol{\alpha} = \boldsymbol{\beta}$ and zero otherwise. Depending on the PDF $\varrho_{\boldsymbol{\theta}}$, the orthonormal polynomials are chosen according to the Wiener-Askey scheme [82] or are constructed numerically [83, 84].

For practical purposes, the PCE is truncated after a finite number of terms P . Typically, one retains the polynomials $\Psi_{\boldsymbol{\alpha}}$ such that a given q -norm of $\boldsymbol{\alpha}$ is not greater than a positive integer s , i.e., for $q \in (0, 1]$

$$\|\boldsymbol{\alpha}\|_q = \left(\sum_{i=1}^d \alpha_i^q \right)^{1/q} \leq s, \quad s \in \mathbb{Z}_{\geq 0}, \quad (16)$$

which yields the following approximation of Eq. (15)

$$\widetilde{\mathcal{M}}(\boldsymbol{\theta}) = \sum_{\|\boldsymbol{\alpha}\|_q \leq s} \mathbf{a}_{\boldsymbol{\alpha}} \Psi_{\boldsymbol{\alpha}}(\boldsymbol{\theta}) \quad (17)$$

The choice of q plays a central role in the construction of the PCE, as it defines which polynomials and corresponding coefficients form the PCE. The most common choice, as well as the one employed in this work, is that of a total-degree polynomials, i.e., $\|\boldsymbol{\alpha}\|_1 \leq s$. In this case, the number of PCE terms is $P = \frac{(s+d)!}{s!d!}$. Since the size of the PCE increases rapidly with both d and s , for high-dimensional input random variables $\boldsymbol{\theta}$, several sparse PCE algorithms have been proposed in the literature to mitigate the impact of the curse of dimensionality [15, 16, 85–88].

The PCE coefficients in Eq. (17) can be computed using several approaches such as the pseudo-spectral projection [18, 89–91], interpolation [92, 93], and, most commonly, regression [15–17, 86–88, 94, 95] where the PCE coefficients are computed by solving a least-squares problem [96]. Consider the indices $\{\boldsymbol{\alpha}_0, \dots, \boldsymbol{\alpha}_{P-1}\}$ and the $P \times n$ coefficient matrix $\mathbf{C} = [\mathbf{a}_{\boldsymbol{\alpha}_0}, \dots, \mathbf{a}_{\boldsymbol{\alpha}_{P-1}}]^\top$. For a set of realizations $\boldsymbol{\Theta} = \{\boldsymbol{\theta}_i\}_{i=1}^N$ with corresponding model outputs $\mathbf{Y} = \{\mathcal{M}(\boldsymbol{\theta}_i)\}_{i=1}^N$, the coefficients are estimated by the solution of:

$$\min_{\mathbf{C} \in \mathbb{R}^{P \times n}} \left\{ \sum_{i=1}^N \left(\mathcal{M}(\boldsymbol{\theta}_i) - \sum_{\|\boldsymbol{\alpha}\|_q \leq s} \mathbf{a}_{\boldsymbol{\alpha}} \Psi_{\boldsymbol{\alpha}}(\boldsymbol{\theta}_i) \right)^2 \right\} \quad (18)$$

which admits the closed form solution

$$\hat{\mathbf{C}} = \left(\mathbf{\Psi}^\top \mathbf{\Psi} \right)^{-1} \mathbf{\Psi}^\top \mathbf{Y} \quad (19)$$

where $\mathbf{\Psi}$ is the matrix containing evaluations of the basis polynomials, that is $\mathbf{\Psi} = \{\psi_{\alpha_j}(\boldsymbol{\theta}_i), \quad 1 \leq i \leq \mathcal{N}, \quad 0 \leq j \leq P - 1\}$. However, the sample size N must be greater than P to make this problem well-posed. To overcome this limitation, estimation of the PCE coefficients can be performed by solving a regularized least squares problem, referred to as the LASSO (least absolute shrinkage and selection operator). The LASSO method applies to scalar response quantities. Hence, in our case, it must be applied successively to every response component individually.

4.2. PCE in local latent spaces

Next, we train n_c PCEs (one for each cluster) to approximate the reduced solution for any new realization of the random vector $\boldsymbol{\theta}$. In cluster C_h , with $h = 1, \dots, n_c$, (which contains N_h points), the truncated PCA of matrix $\mathbf{\Gamma}^{u,v}$ is given by

$$\hat{\mathbf{\Gamma}}^u = \bar{\mathbf{\Gamma}}^u + \sum_{r=1}^{d_u} \mathbf{B}_r^u \boldsymbol{\xi}_r \quad (20a)$$

$$\hat{\mathbf{\Gamma}}^v = \bar{\mathbf{\Gamma}}^v + \sum_{r=1}^{d_v} \mathbf{B}_r^v \boldsymbol{\phi}_r \quad (20b)$$

where $\bar{\mathbf{\Gamma}}^{u,v} = \mathbb{E}[\mathbf{\Gamma}_r^{u,v}]$ is the matrix containing the sample mean-vector and $\mathbf{B}_r^{u,v}$ is the projection of each vector $\mathbf{\Gamma}_r^{u,v}$ onto the corresponding basis given by

$$\mathbf{B}_r^u = \boldsymbol{\xi}_r^\top \left(\mathbf{\Gamma}_r^u - \mathbb{E}[\mathbf{\Gamma}_r^u] \right) \quad (21a)$$

$$\mathbf{B}_r^v = \boldsymbol{\phi}_r^\top \left(\mathbf{\Gamma}_r^v - \mathbb{E}[\mathbf{\Gamma}_r^v] \right) \quad (21b)$$

However, as the response of the model $\mathcal{M}(\boldsymbol{\theta})$ is uncertain, $\mathbf{B}_r^{u,v}$ is function of the input random vector $\boldsymbol{\theta}$ and is therefore a random variable. We seek an estimator $\hat{\mathbf{B}}_r^{u,v}$ using a

truncated PCE as

$$\hat{\mathbf{B}}_r^{u,v}(\boldsymbol{\theta}) = \sum_{\|\boldsymbol{\alpha}_{u,v}\|_q \leq s} \mathbf{a}_{\boldsymbol{\alpha}_{u,v}} \Psi_{\boldsymbol{\alpha}_{u,v}}(\boldsymbol{\theta}) \quad (22)$$

4.3. Out-of-sample extension

Next, consider that we aim to predict the solution for a new realization of the input random variable, $\boldsymbol{\theta}^*$. In the previous step, we constructed n_c PCEs to estimate the coefficients $\hat{\mathbf{B}}^{u,v}$. For the given new sample, we first must determine which PCE model to use. To do so, we identify the nearest² training sample from $\{\boldsymbol{\theta}_i\}_{i=1}^{\mathcal{N}}$ to $\boldsymbol{\theta}^*$ based on the Euclidean distance as

$$\boldsymbol{\theta}_{\text{index}} = \arg \min_{\boldsymbol{\theta}_i} (\|\boldsymbol{\theta}^* - \boldsymbol{\theta}_i\|_2), \quad i = 1, \dots, \mathcal{N}. \quad (23)$$

We then use the PCE for the cluster containing $\boldsymbol{\theta}_{\text{index}}$ to predict the PGA coefficients $\hat{\mathbf{B}}^{u,v}(\boldsymbol{\theta}^*)$ using Eq. (22) and the tangent vectors are approximated by

$$\tilde{\boldsymbol{\Gamma}}^u(\boldsymbol{\theta}^*) = \bar{\boldsymbol{\Gamma}}^u + \sum_{r=1}^{d_u} \hat{\mathbf{B}}_r^u(\boldsymbol{\theta}^*) \boldsymbol{\xi}_r, \quad (24a)$$

$$\tilde{\boldsymbol{\Gamma}}^v(\boldsymbol{\theta}^*) = \bar{\boldsymbol{\Gamma}}^v + \sum_{r=1}^{d_v} \hat{\mathbf{B}}_r^v(\boldsymbol{\theta}^*) \boldsymbol{\phi}_r. \quad (24b)$$

To construct the approximate high-dimensional solution $\tilde{\mathbf{y}}^* = \tilde{\mathcal{M}}(\boldsymbol{\theta}^*)$ and map to the original (physically interpretable) space ($\mathbb{R}^{m_f \times n_f}$), we first perform the exponential mappings:

$$\tilde{\mathbf{U}}(\boldsymbol{\theta}^*) = \text{Exp}_{\hat{\boldsymbol{\mu}}_{\mathbf{U},h}}(\tilde{\boldsymbol{\Gamma}}^u(\boldsymbol{\theta}^*)) \quad (25a)$$

$$\tilde{\mathbf{V}}(\boldsymbol{\theta}^*) = \text{Exp}_{\hat{\boldsymbol{\mu}}_{\mathbf{V},h}}(\tilde{\boldsymbol{\Gamma}}^v(\boldsymbol{\theta}^*)) \quad (25b)$$

²Note, that we could identify more than one nearest training samples and use an ensemble of the corresponding trained PCEs to predict the solution. However, in this case consistency issues arise due to the different dimension across clusters. We will investigate the issue of consistency in future work.

that project the points from the tangent space onto their corresponding Grassmann manifolds. We further construct a PCE approximation of the matrix containing the singular values as:

$$\tilde{\Sigma}(\boldsymbol{\theta}^*) = \sum_{\|\boldsymbol{\alpha}_\Sigma\|_q \leq s} \mathbf{a}_{\boldsymbol{\alpha}_\Sigma} \Psi_{\boldsymbol{\alpha}_\Sigma}(\boldsymbol{\theta}^*) \quad (26)$$

Finally, we use the inverse SVD to obtain a prediction of the full-field solution as:

$$\tilde{\mathbf{y}}^* = \tilde{\mathbf{U}}(\boldsymbol{\theta}^*) \tilde{\Sigma}(\boldsymbol{\theta}^*) \tilde{\mathbf{V}}^\top(\boldsymbol{\theta}^*) \quad (27)$$

To assess the accuracy of predictions from the proposed method, we will use the following two scalar metrics [75]. The first scalar metric is the relative L_2 error in the original space given by

$$L_2(\tilde{\mathbf{y}}^*, \mathbf{y}^*) = \frac{\|\tilde{\mathbf{y}}^* - \mathbf{y}^*\|_2}{\|\mathbf{y}^*\|_2}, \quad (28)$$

where \mathbf{y}^* is the reference response. The second scalar metric is the coefficient of determination (i.e., the R^2 score) given by:

$$R^2 = 1 - \frac{\sum_{i=1}^{n_{dof}} (\tilde{\mathbf{y}}_i^* - \mathbf{y}_i^*)^2}{\sum_{i=1}^{n_{dof}} (\mathbf{y}_i^* - \bar{\mathbf{y}}^*)^2}, \quad (29)$$

where $n_{dof} = m_f \times n_f$ is the size of the model solution and $\bar{\mathbf{y}}^*$ is the mean reference response. A summary of the steps of the proposed method is given in [Appendix B](#).

5. Applications

In this section, we apply the proposed method to a diverse set of problems of increasing complexity. The first example aims to provide an intuitive understanding of the complex low-dimensional representations through a simple low-dimensional problem that can be interpreted graphically. The subsequent examples aim to demonstrate the breadth of high-dimensional problems that can be solved using the proposed approach.

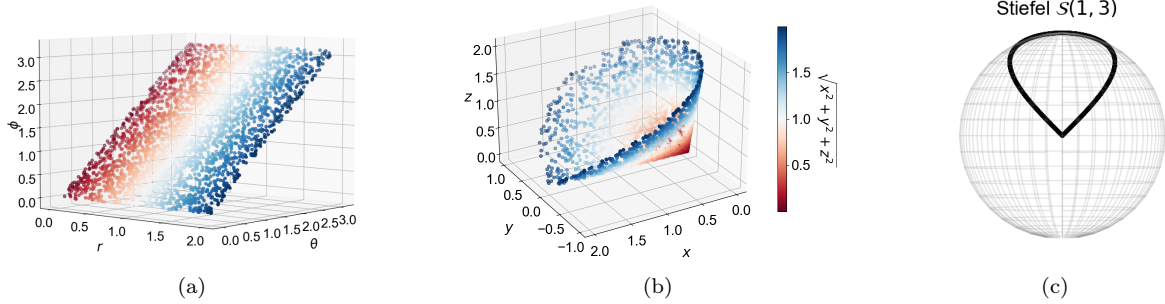


Figure 3: Points on the hypersphere: (a) Realizations of $\boldsymbol{\theta}$. (b) Corresponding realizations of the responses \mathbf{y} . (c) Representation of the points on the Stiefel manifold $\mathbb{S}(1, 3)$

5.1. Points on the hypersphere

In the first example, we use the proposed approach to learn the mapping between points (ϕ, θ, r) defined in polar coordinates and their Cartesian counterparts, that is

$$\begin{aligned}
 x &= r \cos(\phi) \cos(\theta) \\
 y &= r \cos(\phi) \sin(\theta) \\
 z &= r \sin(\phi)
 \end{aligned} \tag{30}$$

Vector $\boldsymbol{\theta} = [r, \theta, \phi]$ is considered to be stochastic with each variable following a uniform probability distribution within a specific range, such that

$$\theta = U[0, \pi], \quad \phi = \theta, \quad r = U[0, 2] \tag{31}$$

The response, i.e., the corresponding Cartesian point $\mathbf{y} = [x, y, z]^\top$, lies in the three-dimensional Euclidean space, \mathbb{R}^3 . The SVD $\mathbf{y} = \mathbf{U}\boldsymbol{\Sigma}\mathbf{V}^\top$ gives $\mathbf{U} \in \mathbb{S}(1, 3)$ which is a point in three-dimensional space that lies on the surface of a unit sphere (Stiefel manifold $\mathcal{St}(1, 3)$), while $\boldsymbol{\Sigma}, \mathbf{V} \in \mathbb{R}$. Figure 3(a-c) shows 3000 realizations of the parameters vector $\boldsymbol{\theta} = [r, \theta, \phi]$, the corresponding realizations of \mathbf{y} , and their representations \mathbf{U} on the Stiefel manifold $\mathcal{St}(1, 3)$, respectively.

We consider training data sets consisting of $\mathcal{N} = 50, 100, 150,$ and 200 training points, i.e., pairs $\{\boldsymbol{\theta}_i, \mathbf{y}_i\}_{i=1}^{\mathcal{N}}$. To evaluate the performance of the surrogate, we generate a test data set of size $\mathcal{N}_* = 3000$. We perform Riemannian K-means to identify groups of points $\{\mathbf{U}_i\}_{i=1}^{N_h}$ that

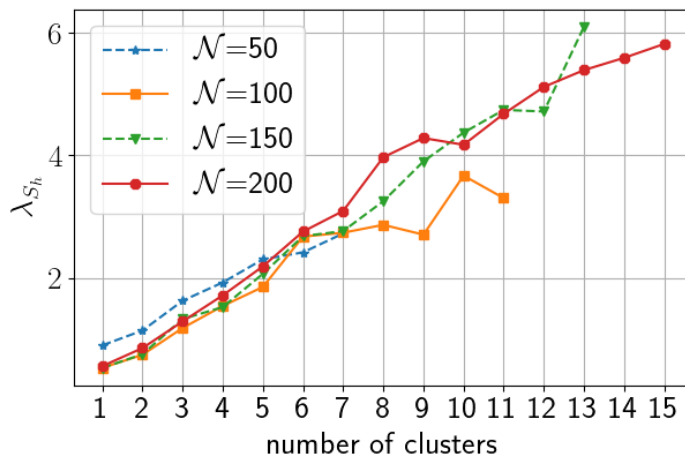


Figure 4: Convergence of the Silhouette coefficient for an increasing number of clusters and for training data sets of increasing size \mathcal{N} . The optimum number of clusters is the one corresponding to the maximum peak of the each plot.

are close on the Stiefel manifold $St(1, 3)$. Figures 4 shows the convergence of the Silhouette coefficient as a function of the number of clusters for increasing number of training points. The optimum number of clusters is the one corresponding to the maximum peak of the each plot. A set requirement is that each cluster contains at least five points. In Figure 5(a) we show $\mathcal{N} = 200$ train points on the sphere divided into 15 clusters, where each color represents a cluster. For two of the clusters we show the tangent vectors that align with the first and second principal geodesic components.

PCE surrogates that map from \mathbf{x} to \mathbf{U} are then constructed, with a maximum polynomial degree p_{\max} that varies from 1 to 3. Figures 5(b-c) visualizes the performance of the PCE surrogate for $p_{\max} = 2$ and $\mathcal{N} = 200$ training points: More specifically, Fig. 5(b) depicts 150 predicted values on the sphere $St(1, 3)$ while Fig. 5(c) shows the predicted full solutions in the Cartesian space. We see that no discrepancies can be observed between the surrogate prediction and the exact solution. This performance of the surrogate is reflected on very low L_2 errors and high R^2 scores for $p_{\max} = 2$ and $p_{\max} = 3$, even for the smallest training data sets. As would be expected, the approximation accuracy in general increases if larger training data sets are employed. This can be attributed to an overfitted PCE and shows clearly that

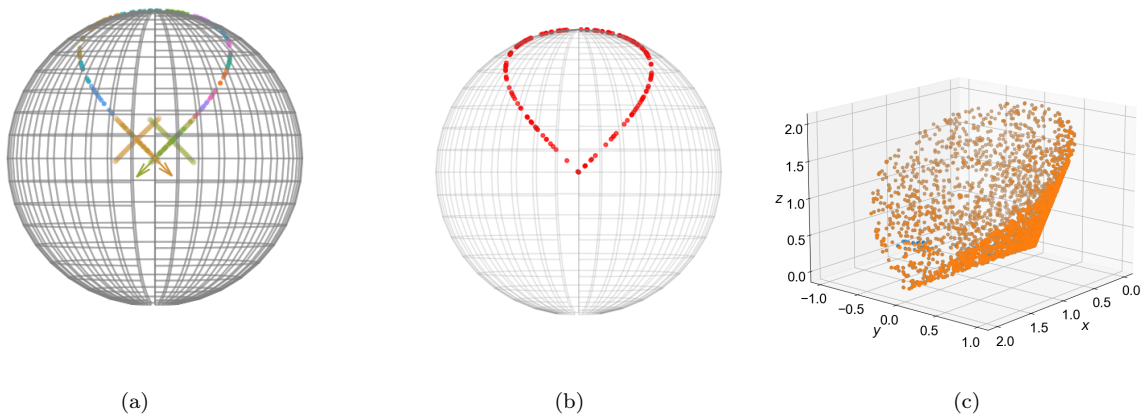


Figure 5: Points on the hypersphere: (a) Cluster of points on $\mathbb{S}(1, 3)$; for two clusters we plot the geodesics on the sphere corresponding to the first and second principal components (b) 150 PCE predicted points on $\mathbb{S}(1, 3)$, (c) and the corresponding solutions in Cartesian space.

p_{\max} must be chosen in accordance to the available training data.

5.2. Lotka-Volterra Dynamical System

In this example, we consider the Lotka-Volterra system of equations [97], a system of first-order non-linear ordinary differential equations (ODEs) used to model the interactions between predators and prey. The model is defined as

$$\begin{aligned} \frac{du}{dt} &= \alpha u - \beta uv, \\ \frac{dv}{dt} &= \delta uv - \gamma v, \end{aligned} \tag{32}$$

where u and v are the prey and predator populations, respectively. The model parameters α , β , γ , and δ are described in Table 1. In our setting, we consider the parameters α and β to be stochastic with values sampled from uniform probability distributions that lie between certain bounds, while parameters γ and δ have fixed values. The initial conditions for the state variables are set to $u_0 = 10$ prey and $v_0 = 5$ predators.

Our goal is to predict the trajectory of both predator and prey species over time using the PGA-PCE surrogate. For each realization θ_i of the vector $[\alpha, \beta] \in \mathbb{R}^2$, we solve the Lotka-Volterra system using a fourth-order Runge-Kutta method with period $T = 25$,

Table 1: Description of the parameters of the Lotka-Volterra equations.

Parameters	Notation	Uncertainty/value
Population of prey species	u	$u_0 = 10$
Population of predator species	v	$v_0 = 5$
Natural growing rate of prey when no predator exists	α	$U(0.90, 1)$
Natural dying rate of prey due to predation	β	$U(0.10, 0.15)$
Natural dying rate of predator when no prey exists	γ	1.50
Reproduction rate of predators per prey eaten	δ	0.75

discretized in 512 points. Therefore, the response of the system $\mathbf{y}_i = [\mathbf{u}_i, \mathbf{v}_i]$ is a point lying in $\mathbb{R}^{2 \times 512}$. The objective is to learn the mapping $\boldsymbol{\theta} \rightarrow \mathbf{y}$ using a small number of training data $\{\boldsymbol{\theta}_i, \mathbf{y}_i\}$. Each response is factorized into three matrices $\mathbf{y}_i \rightarrow \mathbf{U}_i, \boldsymbol{\Sigma}_i, \mathbf{V}_i^T$ using thin SVD. Matrices U_i and V_i correspond to points on the Stiefel manifolds $\mathcal{St}_U(n_1, p) \equiv \mathcal{St}_U(2, 512)$ and $\mathcal{St}_V(n_2, p) \equiv \mathcal{St}(2, 2)$, respectively. Matrix $\boldsymbol{\Sigma}_i$ is a vector in the Euclidean space $\mathbb{R}^p \equiv \mathbb{R}^2$.

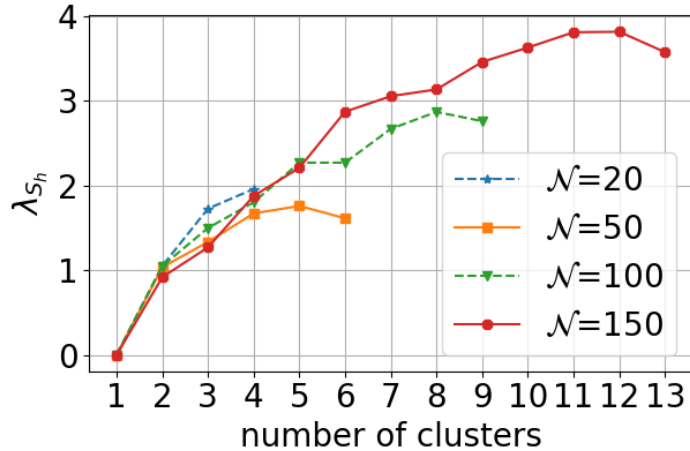


Figure 6: Convergence of the Silhouette coefficient for an increasing number of clusters and for training data sets of increasing size \mathcal{N} . The optimum number of clusters is the one corresponding to the maximum peak of the each plot.

Figure 6 depicts the convergence of the Silhouette coefficient for an increasing number of clusters and for training data sets of increasing size \mathcal{N} . The optimum number of clusters is the one corresponding to the maximum peak of the each plot., i.e., $\mathcal{N} \in \{20, 50, 100, 150\}$. For each training data set size \mathcal{N} , the number of clusters increases progressively, up to the

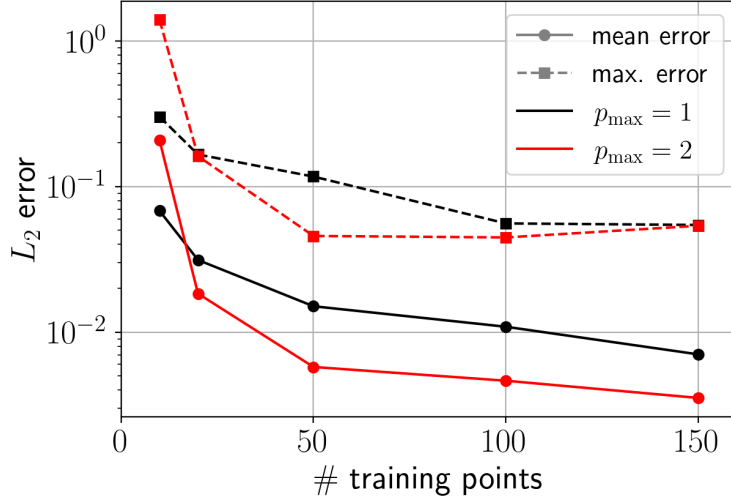


Figure 7: \mathcal{Y} prediction.

Figure 8: Lotka-Volterra: L_2 errors of the surrogate model’s predictions for the QoI \mathcal{Y} , for training data sets of increasing size. The L_2 errors have been computed using a validation data set with $\mathcal{N}_* = 5000$ data points.

point where the optimal number of clusters is identified, as described in Algorithm 2. For $\mathcal{N} = 100$, the optimal number of clusters is 12. In this example, the set requirement is that all clusters contain at least 5 data points. In each cluster, PGA provides a set of principal components -the optimal number of principal components explains 99% of the variance in the data. As expected, different number of principal components is required to achieve a uniformly explained variance across all clusters. For $\mathcal{N} = 150$, the required number of principal components identified in each cluster is 1.

Next, a PCE is constructed for each cluster, and the maximum polynomial degree is set $p_{\max} = 1$ (linear regression) or $p_{\max} = 2$ across the clusters. By identifying the optimal number of clusters in a way that minimizes the variance within each cluster, in the case of small data, a small polynomial degree (i.e., $p_{\max} \leq 3$) will be sufficient. Figure 8 depicts the performance of the surrogate models in terms of the average and maximum L_2 errors, where the latter are computed using a validation data set of size $\mathcal{N}_* = 5000$. More specifically, the surrogate’s predictions of the solutions $\tilde{\mathbf{y}} = \tilde{\mathbf{U}}\tilde{\Sigma}\tilde{\mathbf{V}}^\top$ are compared to the true ones, for training data sets of increasing size. It can be observed that even with 50 training data, the performance of the surrogate can already be considered very good, while additional training

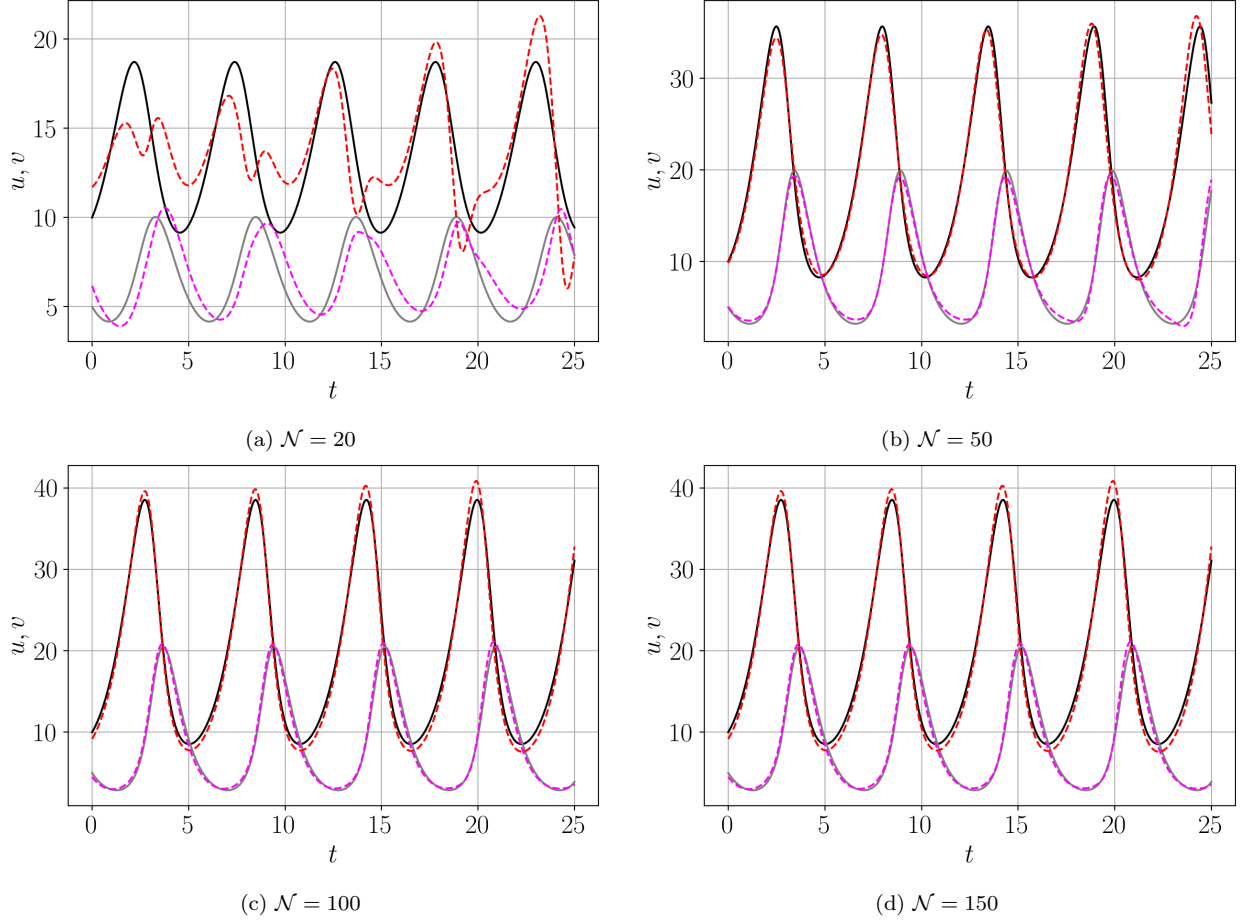
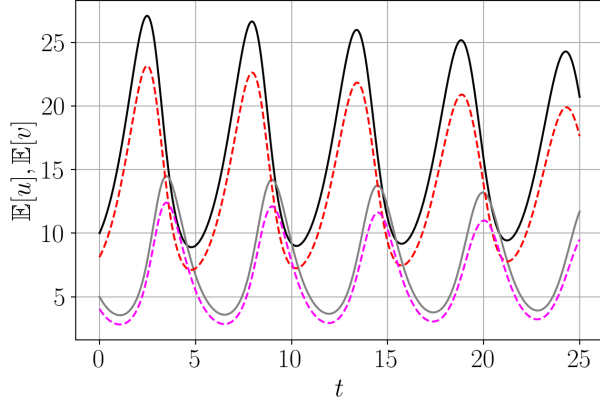


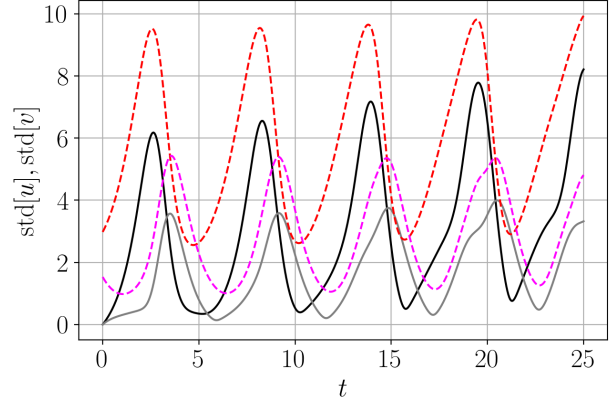
Figure 9: Lotka-Volterra: Worst-case surrogate model predictions for the trajectories of the prey (u) and predator (v) species for increasing number of training samples and $p_{\max} = 2$. The true trajectories are given with solid lines (u : black, v : gray), while the surrogate’s predictions are given with dashed lines (u : red, v : magenta).

data improve the surrogate’s accuracy further.

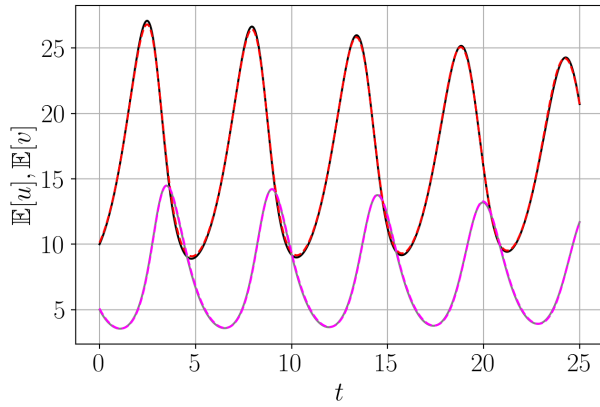
As further verification with respect to the accuracy of the surrogate model, particularly considering data sets of limited size, Figure 9 presents the worst-case predictions of the surrogate model regarding the evolution of the prey and predator species. The worst-case approximations correspond to the maximum L_2 error computed out of the $\mathcal{N}_* = 5000$ validation data. It is obvious that $\mathcal{N} = 20$ training data points are insufficient for an acceptable worst-case prediction, which however is not surprising. A significant improvement is observed already for $\mathcal{N} = 50$ training data where even the worst-case prediction of the surrogate matches the true trajectories very closely.



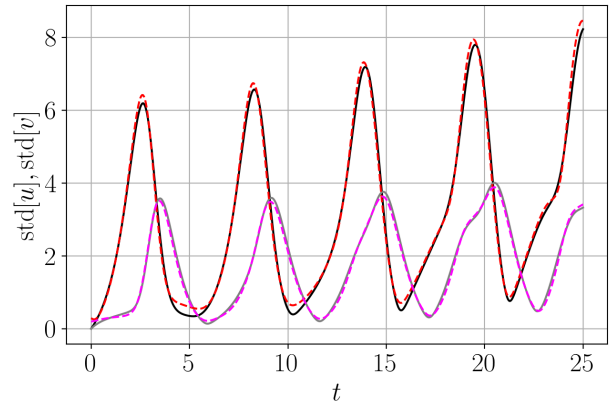
(a) Mean, $\mathcal{N} = 20$.



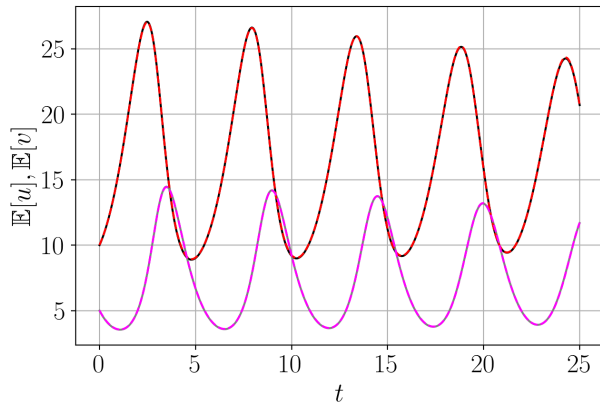
(b) Standard deviation, $\mathcal{N} = 20$.



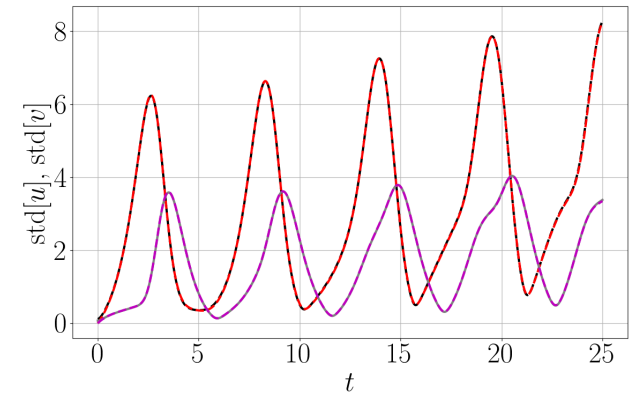
(c) Mean, $\mathcal{N} = 50$.



(d) Standard deviation, $\mathcal{N} = 50$.



(e) Mean, $\mathcal{N} = 150$.



(f) Standard deviation, $\mathcal{N} = 150$.

Figure 10: Lotka-Volterra: Moment estimation for the trajectories of the prey (u) and predator (v) species. The means and standard deviations computed with the true model are given with solid lines (u : black, v : gray), while the surrogate-based estimations (for $p_{\max} = 2$) are given with dashed lines (u : red, v : magenta).

Last, using the same $N_* = 5000$ test realizations, we perform moment estimation via Monte Carlo sampling. Figure 10 shows the mean and the standard deviation of both predator and prey species over time, computed using both the original model and the proposed surrogate. In the latter case, we choose for $p_{\max} = 2$. Looking at the mean trajectories and the corresponding standard deviations, it can be seen that the surrogate-based moment estimation is very accurate with as little as $\mathcal{N} = 50$ training data points, where only minor discrepancies can be observed in comparison to the moments computed using the true model. For $\mathcal{N} = 150$ training data points, surrogate-based estimation of the mean and the standard deviation is almost indistinguishable to the ones computed with the original model.

5.3. Continuous stirred-tank reactor

The continuous stirred-tank reactor (CSTR) is a chemical reactor model that is commonly used in chemical and process engineering modeling and design applications [98]. We consider an ideal CSTR with first-order reaction kinetics and a single reagent. The corresponding concentration and energy balances with respect to the contents of the reactor are given by the system of ODEs

$$\begin{aligned} V \frac{dc}{dt} &= q(c_f - c) - V k(T)c, \\ V \rho C_p \frac{dT}{dt} &= w C_p (T_f - T) + (-\Delta H_R) V k(T)c + U A (T_c - T), \end{aligned} \tag{33}$$

where $k(T) = k_0 \exp(-E_a/RT)$ is the rate constant according to Arrhenius law. All other model parameters are listed in Table 2. As uncertain parameter, we consider the cooling temperature T_c , which is chosen to follow a uniform distribution in the range of [305, 310] K. The system is solved with an explicit Runge-Kutta method of fourth order, with time step equal to 0.01 minutes and for a total duration of 5 minutes. The initial conditions are $c_0 = 0.5$ gmol/lit and $T_0 = 350$ K. The QoIs are the concentration c and the temperature T over time, both of which are extremely sensitive to changes in the cooling temperature. With the given time discretization, the full response of the CSTR model $\mathcal{Y}_i = [\mathbf{c}_i, \mathbf{T}_i]$ is a point lying in $\mathbb{R}^{2 \times 500}$.

Surrogate models with respect to the matrices \mathbf{U} , \mathbf{V} , and $\mathbf{\Sigma}$, as well as for the QoI \mathcal{Y} are constructed using training data sets of size $\mathcal{N} \in \{20, 50, 100\}$ and $p_{\max} = 2$. Otherwise, the surrogate modeling procedure is similar to the one described in Section 5.2. In this case, the objective is to learn the mapping $T_c \rightarrow \mathcal{Y}$ using a small number of training data $\{T_{c,i}, \mathcal{Y}_i\}$. Despite considering only a single random parameter, the surrogate modeling task remains challenging due to the sensitivity of both temperature and reagent concentration to the cooling temperature.

Figure 11 shows the convergence of the Silhouette coefficient for an increasing number of clusters and for training data sets of size $\mathcal{N} = 50$ and $\mathcal{N} = 100$. For $\mathcal{N} = 100$, 17 clusters are required.

Figure 12 shows the surrogate model’s L_2 error with respect to \mathbf{U} , \mathbf{V} , $\mathbf{\Sigma}$, and \mathcal{Y} , computed using a test data set with $\mathcal{N}_* = 5000$ data points. Interestingly, while the L_2 error regarding the QoI \mathcal{Y} decreases monotonically for increasing training data, in two cases, namely, for the matrices \mathbf{U} and $\mathbf{\Sigma}$, the maximum error stagnates or even deteriorates, e.g., for the surrogate’s predictions of $\mathbf{\Sigma}$ with $\mathcal{N} = 50$ training data points. Figure 13 shows the worst-case surrogate model predictions with respect to the concentration and the temperature, out of the aforementioned $\mathcal{N}_* = 5000$ test model evaluations. As can be observed, with

Table 2: Parameters of the CSTR model.

Parameters	Notation	Uncertainty/value
Reagent concentration (gmol/lit)	c	$c_0 = 0.5$
Feed concentration (gmol/lit)	c_f	1.0
Temperature (K)	T	$T_0 = 350$
Feed temperature (K)	T_f	350
Cooling temperature (K)	T_c	$U(305, 310)$
Activation energy (J/gmol)	E_a	72750
Pre-exponential factor (1/min)	k_0	$7.2 \cdot 10^7$
Gas constant (J/kmol/K)	R	8.314
Reactor volume (lit)	V	100
Density (g/lit)	ρ	1000
Heat capacity (J/g/K)	C_p	0.239
Reaction enthalpy (J/gmol)	ΔH_R	$-5 \cdot 10^4$
Heat transfer coefficient (J/min/K)	UA	$5 \cdot 10^4$
Feed flowrate (lit/min)	q	100

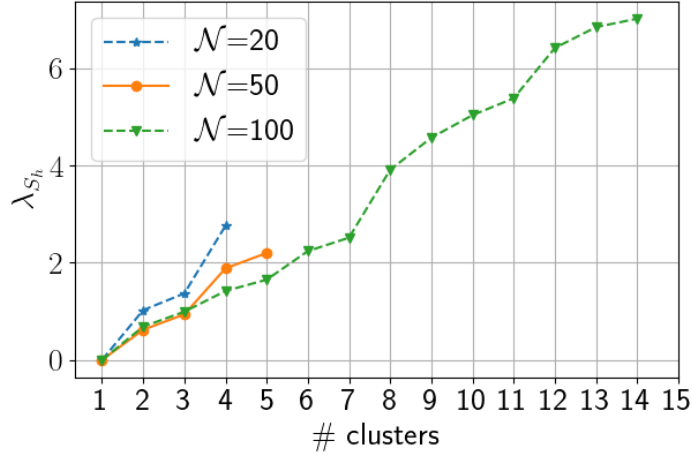


Figure 11: Convergence of the Silhouette coefficient for an increasing number of clusters and for training data sets of increasing size \mathcal{N} . The optimum number of clusters is the one corresponding to the maximum peak of the each plot since the minimum number of points ($N_h = 5$) allowed within a cluster was reached.

$\mathcal{N} = 50$ training data points, the surrogate’s prediction captures the correct physical behavior, however, without sufficient accuracy. For $\mathcal{N} = 100$ training data points, the accuracy of the surrogate increases significantly and only minor differences to the true model can be observed, even in the worst case.

Last, Figure 14 shows the surrogate-based estimations for standard deviation of c and T over time, in comparison to the estimations based on the true CSTR model. Similar to 5.2, the estimations for the standard deviations is based on Monte Carlo sampling, using the $\mathcal{N}_* = 5000$ original and surrogate model evaluations that were previously employed to compute the L_2 error metrics and the worst-case predictions of the surrogate. The estimations for the mean trajectories of c and T have been omitted, due to the fact that the surrogate’s estimations match those of the true model even for $\mathcal{N} = 20$ training data points. Contrarily, in the case of the standard deviation, differences between the true and the surrogate model can be observed for $\mathcal{N} = 20$ and $\mathcal{N} = 50$ training data points, in particular at the start and end times of the simulation. These differences become negligible if $\mathcal{N} = 100$ data points are used to train the surrogate model.

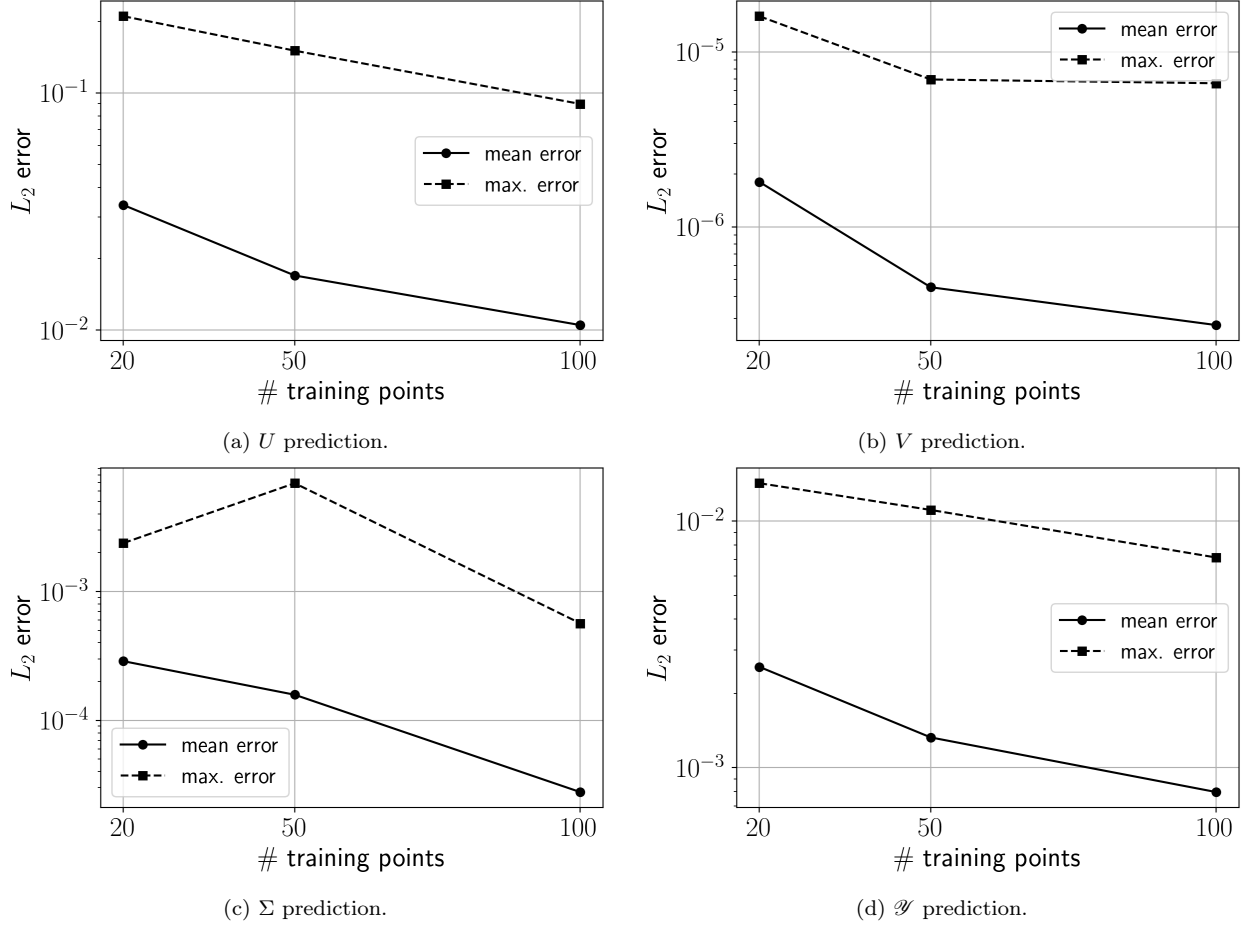


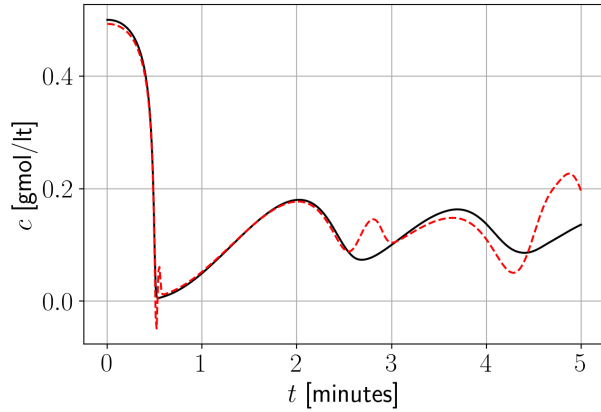
Figure 12: CSTR: L_2 errors of the surrogate model’s predictions with respect to the matrices U , V , and Σ , as well as for the QoI \mathcal{J} , for training data sets of increasing size. The L_2 errors have been computed using a validation data set with $\mathcal{N}_* = 5000$ data points. The PCE surrogates are constructed with $p_{\max} = 2$.

5.4. Rayleigh-Bénard convection

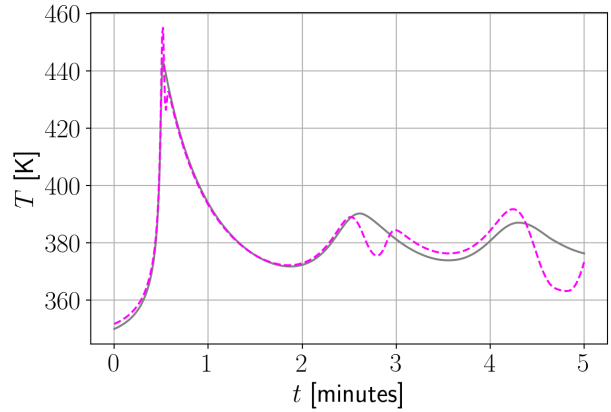
Rayleigh-Bénard convection is a natural phenomenon that occurs in a thin layer of fluid when it is heated from below [99]. It is characterized by the formation of fluid motion patterns driven by buoyancy forces. The convection arises due to a temperature gradient (ΔT) across the fluid layer, with warmer fluid rising and cooler fluid sinking, creating a circulation pattern. The instability in Rayleigh-Bénard convection is determined by the non-dimensional Rayleigh number

$$Ra = \frac{\alpha \Delta T g h^3}{\nu \kappa} \quad (34)$$

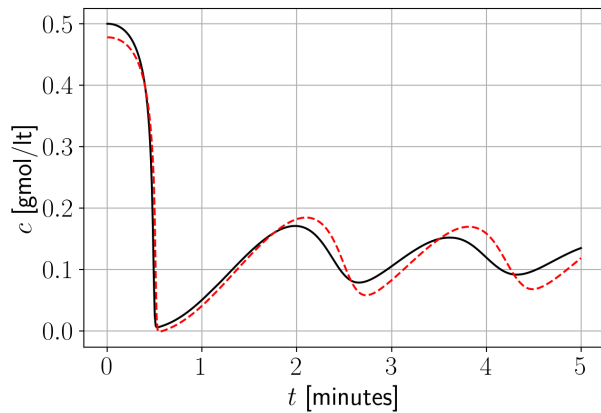
where α is the thermal expansion coefficient, g is the gravitational acceleration, h is



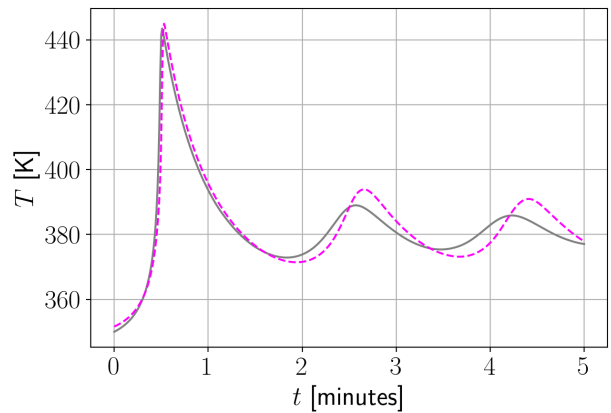
(a) Worst-case concentration, $\mathcal{N} = 20$.



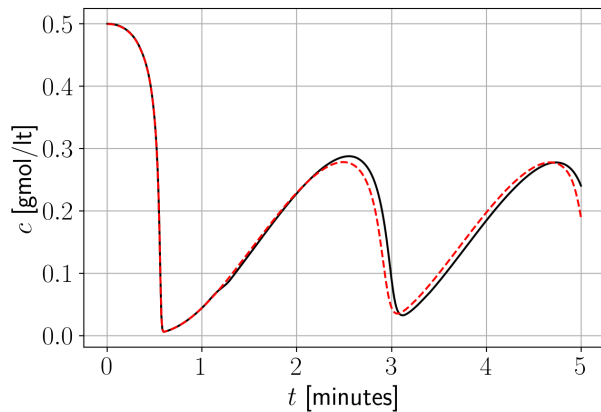
(b) Worst-case temperature, $\mathcal{N} = 20$.



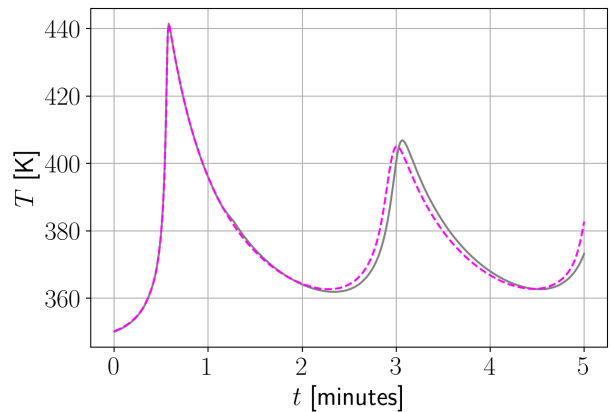
(c) Worst-case concentration, $\mathcal{N} = 50$.



(d) Worst-case temperature, $\mathcal{N} = 50$.

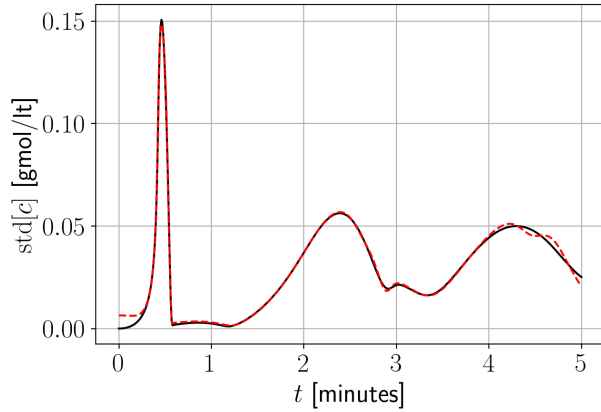


(e) Worst-case concentration, $\mathcal{N} = 100$.

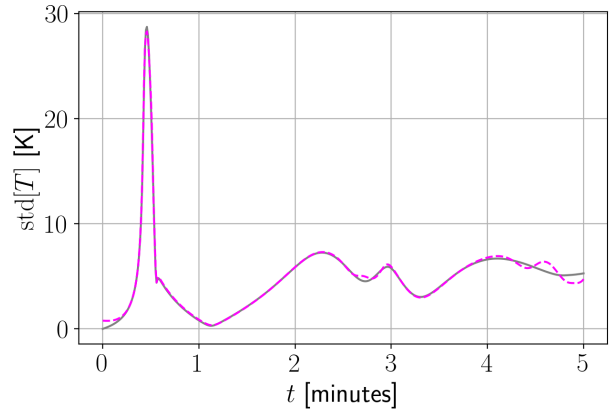


(f) Worst-case temperature, $\mathcal{N} = 100$.

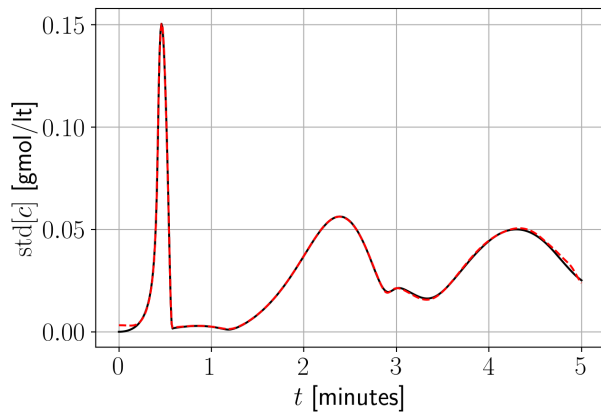
Figure 13: CSTR: Worst-case surrogate model predictions for the concentration and temperature over time. The true trajectories are given with solid lines (c : black, T : gray), while the surrogate's predictions are given with dashed lines (c : red, T : magenta).



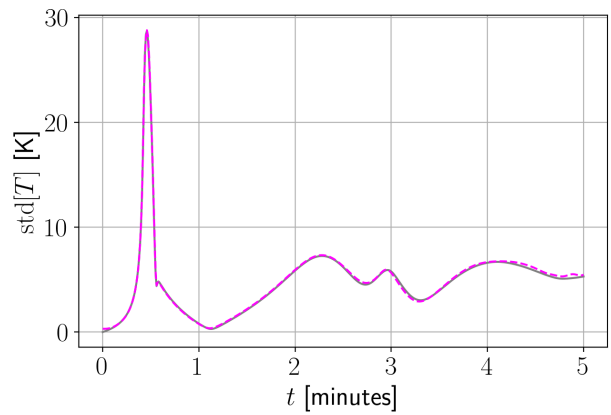
(a) Standard deviation of concentration, $\mathcal{N} = 20$.



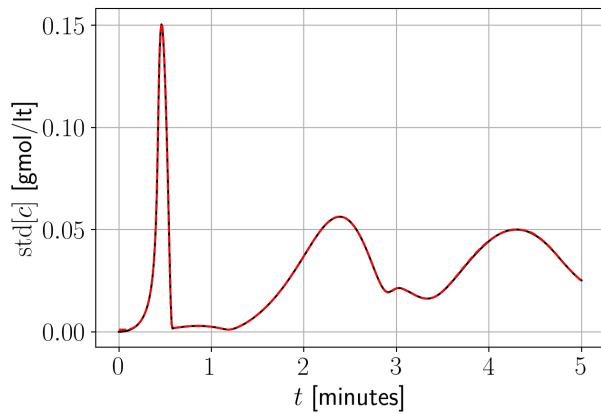
(b) Standard deviation of temperature, $\mathcal{N} = 20$.



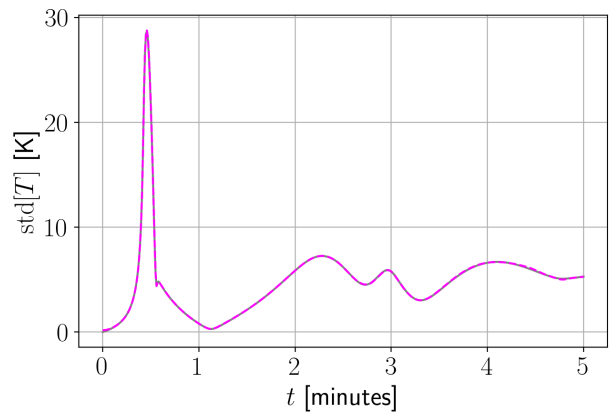
(c) Standard deviation of concentration, $\mathcal{N} = 50$.



(d) Standard deviation of temperature, $\mathcal{N} = 50$.



(e) Standard deviation of concentration, $\mathcal{N} = 100$.



(f) Standard deviation of temperature, $\mathcal{N} = 100$.

Figure 14: CSTR: Standard deviation estimation for the concentration and the temperature over time. The standard deviations computed with the true model are given with solid lines (c : black, T : gray), while the surrogate-based estimations are given with dashed lines (c : red, T : magenta).

the thickness of the fluid layer, ν is the kinematic viscosity and κ is the thermal diffusivity. This number represents the ratio between the buoyancy forces and the viscous forces within the fluid. When the temperature gradient ΔT exceeds a certain threshold, the Rayleigh number surpasses a critical value, leading to the onset of convection and the formation of characteristic patterns, such as thermal plumes or rolls.

The dimensional form of the Rayleigh-Bénard equations for an incompressible fluid defined on a domain Ω can be derived by considering the governing conservation laws for mass, momentum, and energy, along with the Boussinesq approximation, which assumes that density perturbations solely impact the gravitational force.

$$\begin{cases} \frac{d\mathbf{u}}{dt} = -\frac{1}{\rho_0}\nabla p + \frac{\rho}{\rho_0}g + \nu\nabla^2\mathbf{u} & \mathbf{x} \in \Omega, t > 0 \\ \frac{dT}{dt} = \kappa\nabla^2 T & \mathbf{x} \in \Omega, t > 0 \\ \nabla\mathbf{u} = 0 \\ \rho = \rho_0(1 - \alpha(T - T_0)) \end{cases}$$

where $\frac{d}{dt}$ denotes material derivative, \mathbf{u} , p , T are the fluid velocity, pressure and temperature respectively, T_0 is the temperature at the lower plate, and $\mathbf{x} = (x, y)$ are the spatial coordinates. The corresponding boundary and initial conditions are defined, respectively, as

$$\begin{cases} T(\mathbf{x}, t)|_{y=0} = T_0 & \mathbf{x} \in \Omega, t > 0 \\ T(\mathbf{x}, h)|_{y=0} = T_1 & \mathbf{x} \in \Omega, t > 0 \\ \mathbf{u}(\mathbf{x}, h)|_{y=0} = \mathbf{u}(\mathbf{x}, h)|_{y=h} = 0 & \mathbf{x} \in \Omega, t > 0 \\ T(y, t)|_{t=0} = T_0 + \frac{y}{h}(T_1 - T_0) + 0.1\nu(\mathbf{x}) & \mathbf{x} \in \Omega \\ \mathbf{u}(\mathbf{x}, t)|_{t=0} = 0 & \mathbf{x} \in \Omega \end{cases}$$

where T_0 , and T_1 are the fixed temperatures of the lower and upper plates, respectively. The simulation takes place in a domain $\Omega = [0, 4] \times [0, 1]$, discretized with $n_x \times n_y = 128 \times 64$ mesh points. We consider the dimensionless Rayleigh number to be uniformly distributed in the range $[1 \cdot 10^6, 5 \cdot 10^6]$, while the the Prandtl number is equal to 1. For each realization, the partial differential equations is solved in the time interval $t = [0, 20]$ for $\delta t = 0.25$. We want to train our model to predict the response (buoyancy forces) at time $t = 18$. We

generated 200 data from which $\mathcal{N} = 50$ were used for training and $\mathcal{N}^* = 150$ were used for testing. Datasets were generated using the Dedalus Project that can be found in <https://github.com/DedalusProject/dedalus>.

We ran our algorithm and the optimal number of clusters was found to be 7. Figure 15 depicts the best- and worst-case surrogate model predictions with respect to the buoyancy, out of the 150 test model evaluations. As can be observed, even with $\mathcal{N} = 50$ training data points, the surrogate’s prediction captures the correct physical behavior, with only minor differences to the true model can be observed, even in the worst-case.

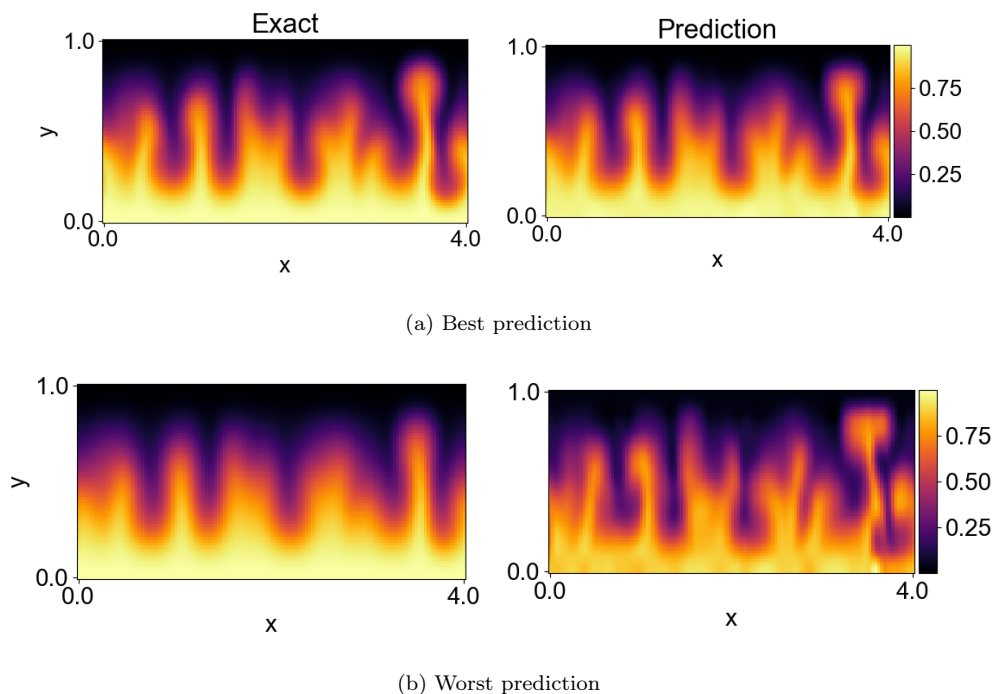
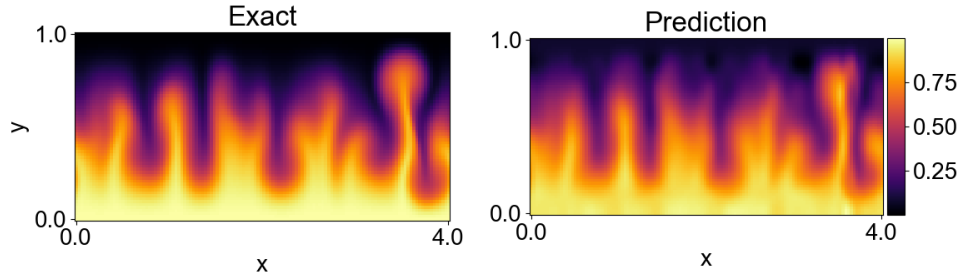
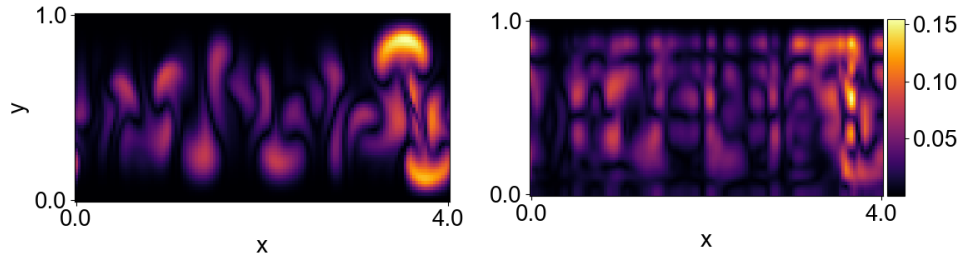


Figure 15: Rayleigh-Bénard: Best-case (first row) and worst-case (second row) surrogate model predictions for the (normalized, non-dimensional) buoyancy vs the reference solution.

Figure 16 shows the surrogate’s estimations for the mean buoyancy field and the standard deviation (based on the $\mathcal{N} = 150$ test points), in comparison to the estimations based on the true model. As we can observe from this figure, the surrogate’s estimations match those of the true model with sufficient accuracy. Similarly, the differences between the true model and the surrogate model in the case of the standard deviation are negligible. These differences are quantified in terms of the L_2 error, depicted in Fig. 17.



(a) Mean



(b) Standard deviation

Figure 16: Rayleigh-Bénard: Relative errors for the mean field and standard deviation surrogate predictions.

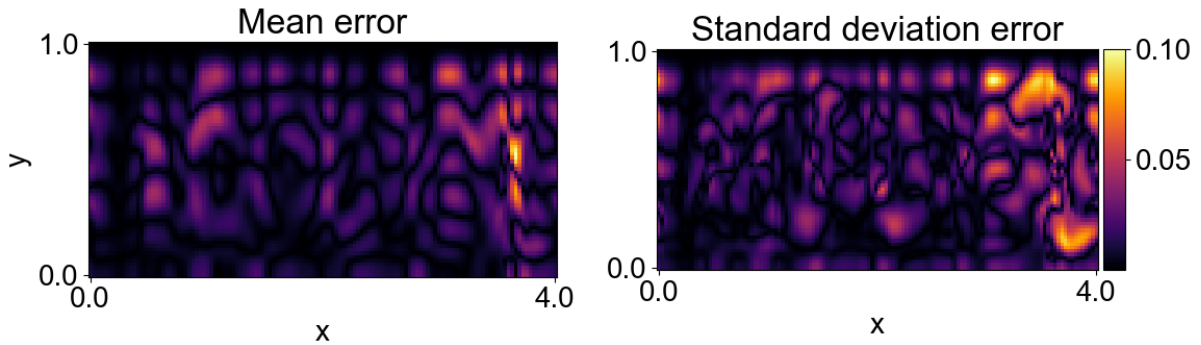


Figure 17: Rayleigh-Bénard: Mean field and standard deviation errors.

6. Discussion and Conclusions

The paper presents a new methodology for creating surrogate models in high-dimensional systems for uncertainty quantification. The method combines Principal Geodesic Analysis on the Grassmann manifold of the response with Polynomial Chaos expansion to construct a mapping between the random input parameters and the projection of the response on the local

principal geodesic submanifolds. The resulting surrogate model uses an adaptive algorithm based on unsupervised learning and the minimization of the sample Fréchet variance on the Grassmann manifold. The method is tested on four applications from different fields and shows promising results for accurately predicting new solutions. Additionally, the method is computationally efficient and reduces the cost associated with high-fidelity simulations. However, the method's computational cost becomes intractable for cases with high-dimensional input parameter spaces, and the use of standard random or quasi-random sampling techniques might not be ideal for all cases. Future research should focus on addressing these limitations and challenges.

References

- [1] Timothy John Sullivan. Introduction to uncertainty quantification. *Springer*, 63, 2015.
- [2] Nicholas Metropolis et al. The beginning of the monte carlo method. *Los Alamos Science*, 15:125–130, 1987.
- [3] Jun S Liu and Jun S Liu. Monte carlo strategies in scientific computing. *Springer*, 10, 2001.
- [4] B. Sudret, S. Marelli, and J. Wiart. Surrogate models for uncertainty quantification: An overview. page 793–797, 2017.
- [5] Bhosekar A. and Ierapetritou M. Advances in surrogate based modeling, feasibility analysis, and optimization: A review. *Computers & Chemical Engineering*, 108:250–267, 2018.
- [6] Xu Wu and Tomasz Kozłowski. Inverse uncertainty quantification of reactor simulations under the bayesian framework using surrogate models constructed by polynomial chaos expansion. *Nuclear Engineering and Design*, 313:29–52, 2017.

- [7] Maliki Moustapha and Bruno Sudret. Surrogate-assisted reliability-based design optimization: a survey and a unified modular framework. *Structural and Multidisciplinary Optimization*, 60:2157–2176, 2019.
- [8] Xiang Sun, Yun Young Choi, and Jung-Il Choi. Global sensitivity analysis for multivariate outputs using polynomial chaos-based surrogate models. *Applied Mathematical Modelling*, 82:867–887, 2020.
- [9] Riccardo Trincherò, Mourad Larbi, Hakki M Torun, Flavio G Canavero, and Madhavan Swaminathan. Machine learning and uncertainty quantification for surrogate models of integrated devices with a large number of parameters. *IEEE Access*, 7:4056–4066, 2018.
- [10] Jiachuan He, Steven A Mattis, Troy D Butler, and Clint N Dawson. Data-driven uncertainty quantification for predictive flow and transport modeling using support vector machines. *Computational Geosciences*, 23:631–645, 2019.
- [11] Ilias Bilonis and Nicholas Zabaras. Multi-output local gaussian process regression: Applications to uncertainty quantification. *Journal of Computational Physics*, 231(17): 5718–5746, 2012.
- [12] Rohit Tripathy, Ilias Bilonis, and Marcial Gonzalez. Gaussian processes with built-in dimensionality reduction: Applications to high-dimensional uncertainty propagation. *Journal of Computational Physics*, 321:191–223, 2016.
- [13] Rohit K Tripathy and Ilias Bilonis. Deep UQ: Learning deep neural network surrogate models for high dimensional uncertainty quantification. *Journal of Computational Physics*, 375:565–588, 2018.
- [14] Shaoxing Mo, Yinhao Zhu, Nicholas Zabaras, Xiaoqing Shi, and Jichun Wu. Deep convolutional encoder-decoder networks for uncertainty quantification of dynamic multiphase flow in heterogeneous media. *Water Resources Research*, 55(1):703–728, 2019.

- [15] Dimitrios Loukrezis, Armin Galetzka, and Herbert De Gersem. Robust adaptive least squares polynomial chaos expansions in high-frequency applications. *International Journal of Numerical Modelling: Electronic Networks, Devices and Fields*, 33(6):e2725, 2020.
- [16] Géraud Blatman and Bruno Sudret. Adaptive sparse polynomial chaos expansion based on least angle regression. *Journal of Computational Physics*, 230(6):2345–2367, 2011.
- [17] Mohammad Hadigol and Alireza Doostan. Least squares polynomial chaos expansion: A review of sampling strategies. *Computer Methods in Applied Mechanics and Engineering*, 332:382–407, 2018.
- [18] Omar M Knio and OP Le Maitre. Uncertainty propagation in CFD using polynomial chaos decomposition. *Fluid Dynamics Research*, 38(9):616, 2006.
- [19] Bruno Sudret. Global sensitivity analysis using polynomial chaos expansions. *Reliability Engineering & System Safety*, 93(7):964–979, 2008.
- [20] Thierry Crestaux, Olivier Le Maitre, and Jean-Marc Martinez. Polynomial chaos expansion for sensitivity analysis. *Reliability Engineering & System Safety*, 94(7):1161–1172, 2009.
- [21] Himanshu Sharma, Michael D. Shields, and Lukáš Novák. Constrained non-intrusive polynomial chaos expansion for physics-informed machine learning regression. In *Proceedings of the 14th International Conference on Applications of Statistics and Probability in Civil Engineering*, Ireland, July 2023.
- [22] Lukáš Novák, Himanshu Sharma, and Michael D Shields. Physics-informed polynomial chaos expansions. *arXiv preprint arXiv:2309.01697*, 2023.
- [23] Nora Lüthen, Stefano Marelli, and Bruno Sudret. Sparse polynomial chaos expansions: Literature survey and benchmark. *SIAM/ASA Journal on Uncertainty Quantification*, 9(2):593–649, 2021.

- [24] Nora Lüthen, Stefano Marelli, and Bruno Sudret. Automatic selection of basis-adaptive sparse polynomial chaos expansions for engineering applications. *International Journal for Uncertainty Quantification*, 12(3), 2022.
- [25] Van den Herik J. Van der Maaten L, Postma E. Dimensionality reduction: A comparative review. *J Mach Learn Res*, 10:66–71, 2009.
- [26] Ronald R Coifman and Stéphane Lafon. Diffusion maps. *Applied and Computational Harmonic Analysis*, 21(1):5–30, 2006.
- [27] Ketson R Dos Santos, Dimitrios G Giovanis, and Michael D Shields. Grassmannian diffusion maps-based dimension reduction and classification for high-dimensional data. *SIAM Journal on Scientific Computing*, 44(2):B250–B274, 2022.
- [28] Mikhail Belkin and Partha Niyogi. Laplacian eigenmaps for dimensionality reduction and data representation. *Neural computation*, 15(6):1373–1396, 2003.
- [29] Mukund Balasubramanian and Eric L Schwartz. The isomap algorithm and topological stability. *Science*, 295(5552):7–7, 2002.
- [30] Dimitris G Giovanis and Michael D Shields. Data-driven surrogates for high dimensional models using gaussian process regression on the Grassmann manifold. *Computer Methods in Applied Mechanics and Engineering*, 370:113269, 2020.
- [31] Dimitris G Giovanis and Michael D Shields. Uncertainty quantification for complex systems with very high dimensional response using Grassmann manifold variations. *Journal of Computational Physics*, 364:393–415, 2018.
- [32] DG Giovanis and MD Shields. Variance-based simplex stochastic collocation with model order reduction for high-dimensional systems. *International Journal for Numerical Methods in Engineering*, 117(11):1079–1116, 2019.
- [33] Christian Soize and Roger Ghanem. Data-driven probability concentration and sampling on manifold. *Journal of Computational Physics*, 321:242–258, 2016.

- [34] Christian Soize and Roger Ghanem. Polynomial chaos representation of databases on manifolds. *Journal of Computational Physics*, 335:201–221, 2017.
- [35] Christian Soize and Roger Ghanem. Probabilistic learning on manifolds constrained by nonlinear partial differential equations for small datasets. *Computer Methods in Applied Mechanics and Engineering*, 380:113777, 2021.
- [36] I Kalogeris and V Papadopoulos. Diffusion maps-based surrogate modeling: An alternative machine learning approach. *International Journal for Numerical Methods in Engineering*, 121(4):602–620, 2020.
- [37] ED Koronaki, AM Nikas, and AG Boudouvis. A data-driven reduced-order model of nonlinear processes based on diffusion maps and artificial neural networks. *Chemical Engineering Journal*, 397:125475, 2020.
- [38] Ketson RM dos Santos, Dimitris G Giovanis, Katiana Kontolati, Dimitrios Loukrezis, and Michael D Shields. Grassmannian diffusion maps based surrogate modeling via geometric harmonics. *International Journal for Numerical Methods in Engineering*, 2022.
- [39] Christos Lataniotis, Stefano Marelli, and Bruno Sudret. Extending classical surrogate modeling to high dimensions through supervised dimensionality reduction: a data-driven approach. *International Journal for Uncertainty Quantification*, 10(1), 2020.
- [40] Katiana Kontolati, Dimitrios Loukrezis, Dimitrios G Giovanis, Lohit Vandanapu, and Michael D Shields. A survey of unsupervised learning methods for high-dimensional uncertainty quantification in black-box-type problems. *Journal of Computational Physics*, 464:111313, 2022.
- [41] Yasi Wang, Hongxun Yao, and Sicheng Zhao. Auto-encoder based dimensionality reduction. *Neurocomputing*, 184:232–242, 2016.
- [42] Waseem Rawat and Zenghui Wang. Deep convolutional neural networks for image classification: A comprehensive review. *Neural Computation*, 29(9):2352–2449, 2017.

- [43] Jan S Hesthaven and Stefano Ubbiali. Non-intrusive reduced order modeling of nonlinear problems using neural networks. *Journal of Computational Physics*, 363:55–78, 2018.
- [44] Shaoxing Mo, Nicholas Zabaras, Xiaoqing Shi, and Jichun Wu. Deep autoregressive neural networks for high-dimensional inverse problems in groundwater contaminant source identification. *Water Resources Research*, 55(5):3856–3881, 2019.
- [45] Nils Thuerey, Konstantin Weißenow, Lukas Prantl, and Xiangyu Hu. Deep learning methods for reynolds-averaged navier–stokes simulations of airfoil flows. *AIAA Journal*, 58(1):25–36, 2020.
- [46] Nanzhe Wang, Haibin Chang, and Dongxiao Zhang. Efficient uncertainty quantification for dynamic subsurface flow with surrogate by theory-guided neural network. *Computer Methods in Applied Mechanics and Engineering*, 373:113492, 2021.
- [47] Lu Lu, Pengzhan Jin, Guofei Pang, Zhongqiang Zhang, and George Em Karniadakis. Learning nonlinear operators via deeponet based on the universal approximation theorem of operators. *Nature machine intelligence*, 3(3):218–229, 2021.
- [48] Zongyi Li, Nikola Kovachki, Kamyar Azizzadenesheli, Burigede Liu, Kaushik Bhattacharya, Andrew Stuart, and Anima Anandkumar. Fourier neural operator for parametric partial differential equations. *arXiv preprint arXiv:2010.08895*, 2020.
- [49] Katiana Kontolati, Somdatta Goswami, Michael D Shields, and George Em Karniadakis. On the influence of over-parameterization in manifold based surrogates and deep neural operators. *Journal of Computational Physics*, 479:112008, 2023.
- [50] Maziar Raissi, Paris Perdikaris, and George E Karniadakis. Physics-informed neural networks: A deep learning framework for solving forward and inverse problems involving nonlinear partial differential equations. *Journal of Computational physics*, 378:686–707, 2019.
- [51] Somdatta Goswami, Aniruddha Bora, Yue Yu, and George Em Karniadakis. Physics-informed neural operators. *arXiv preprint arXiv:2207.05748*, 2022.

- [52] Katiana Kontolati, Darius Alix-Williams, Nicholas M Boffi, Michael L Falk, Chris H Rycroft, and Michael D Shields. Manifold learning for coarse-graining atomistic simulations: Application to amorphous solids. *Acta Materialia*, page 117008, 2021.
- [53] Audrey Olivier, Dimitrios Giovanis, BS Aakash, Mohit Chauhan, Lohit Vandanapu, and Michael D Shields. Uqpy: A general purpose python package and development environment for uncertainty quantification. *Journal of Computational Science*, 47:101204, 2020.
- [54] Dimitrios Tsapetis, Michael D Shields, Dimitris G Giovanis, Audrey Olivier, Lukas Novak, Promit Chakroborty, Himanshu Sharma, Mohit Chauhan, Katiana Kontolati, Lohit Vandanapu, et al. Uqpy v4. 1: Uncertainty quantification with python. *arXiv preprint arXiv:2305.09572*, 2023.
- [55] Nina Miolane, Nicolas Guigui, Alice Le Brigant, Johan Mathe, Benjamin Hou, Yann Thanwerdas, Stefan Heyder, Olivier Peltre, Niklas Koep, Hadi Zaatiti, Hatem Hajri, Yann Cabanes, Thomas Gerald, Paul Chauchat, Christian Shewmake, Daniel Brooks, Bernhard Kainz, Claire Donnat, Susan Holmes, and Xavier Pennec. Geomstats: A python package for riemannian geometry in machine learning. *Journal of Machine Learning Research*, 21(223):1–9, 2020. URL <http://jmlr.org/papers/v21/19-027.html>.
- [56] Nicholas Guigui, Nina Miolane, and Xavier Pennec. Introduction to riemannian geometry and geometric statistics: from basic theory to implementation with geomstats. *Foundations and Trends in Machine Learning*, 16(3):329–493, 2023.
- [57] Alan Edelman, Tomás A Arias, and Steven T Smith. The geometry of algorithms with orthogonality constraints. *SIAM journal on Matrix Analysis and Applications*, 20(2):303–353, 1998.
- [58] P-A Absil, Robert Mahony, and Rodolphe Sepulchre. Riemannian geometry of grassmann manifolds with a view on algorithmic computation. *Acta Applicandae Mathematica*, 80(2):199–220, 2004.

- [59] A. Edelman, T. A. Arias, and S. T. Smith. The geometry of algorithms with orthogonality constraints. *SIAM. J. Matrix Anal. & Appl.*, 20(2):303–353, 1998.
- [60] Zhiwu Huang, Jiqing Wu, and Luc Van Gool. Building deep networks on grassmann manifolds. In *Proceedings of the AAAI Conference on Artificial Intelligence*, volume 32, 2018.
- [61] Yui Man Lui. Advances in matrix manifolds for computer vision. *Image and Vision Computing*, 30(6-7):380–388, 2012.
- [62] Nicolas Boumal and P-A Absil. Low-rank matrix completion via preconditioned optimization on the grassmann manifold. *Linear Algebra and its Applications*, 475:200–239, 2015.
- [63] Boyue Wang, Yongli Hu, Junbin Gao, Yanfeng Sun, and Baocai Yin. Low rank representation on grassmann manifolds. In *Asian conference on computer vision*, pages 81–96. Springer, 2014.
- [64] David Amsallem and Charbel Farhat. Interpolation method for adapting reduced-order models and application to aeroelasticity. *AIAA Journal*, 46(7):1803–1813, 2008.
- [65] Kshitiz Upadhyay, Dimitris G Giovanis, Ahmed Alshareef, Andrew K Knutsen, Curtis L Johnson, Aaron Carass, Philip V Bayly, Michael D Shields, and KT Ramesh. Data-driven uncertainty quantification in computational human head models. *Computer Methods in Applied Mechanics and Engineering*, 398:115108, 2022.
- [66] Jihun Hamm and Daniel D. Lee. Grassmann discriminant analysis: A unifying view on subspace-based learning. In *Proceedings of the 25th International Conference on Machine Learning*, pages 376–383. ACM, 2008.
- [67] K. Ye and L. H. Lim. Schubert varieties and distances between subspaces of different dimensions. *SIAM Journal on Matrix Analysis and Applications*, 37(3):1176–1197, 2016.

- [68] Jihun Hamm and Daniel Lee. Extended grassmann kernels for subspace-based learning. In D. Koller, D. Schuurmans, Y. Bengio, and L. Bottou, editors, *Advances in Neural Information Processing Systems*, volume 21. Curran Associates, Inc., 2008. URL <https://proceedings.neurips.cc/paper/2008/file/e7f8a7fb0b77bcb3b283af5be021448f-Paper.pdf>.
- [69] Paromita Dubey and Hans-Georg Muller. Fréchet analysis of variance for random objects. *Biometrika*, 2017.
- [70] X. Pennec. Probabilities and statistics on riemannian manifolds: basic tools for geometric measurements. in *IEEE Workshop on Nonlinear Signal and Image Processing*, 1999.
- [71] E. Begelfor and M. Werman. Affine invariance revisited. *2006 IEEE Computer Society Conference on Computer Vision and Pattern Recognition (CVPR'06)*, 2:2087–2094, 2006.
- [72] H. Karcher. Riemannian center of mass and mollifier smoothing. *Communications on Pure and Applied Mathematics*, 30:509–541, 2008.
- [73] Hervé Abdi and Lynne J Williams. Principal component analysis. *Wiley interdisciplinary reviews: computational statistics*, 2(4):433–459, 2010.
- [74] P Thomas Fletcher, Conglin Lu, Stephen M Pizer, and Sarang Joshi. Principal geodesic analysis for the study of nonlinear statistics of shape. *IEEE transactions on medical imaging*, 23(8):995–1005, 2004.
- [75] Katiana Kontolati, Dimitrios Loukrezis, Ketson Roberto Maximiano dos Santos, Dimitrios G. Giovanis, and Michael D. Shields. Manifold learning-based polynomial chaos expansions for high-dimensional surrogate models. *ArXiv*, abs/2107.09814, 2021.
- [76] Youshan Zhang. K-means principal geodesic analysis on riemannian manifolds. In Kohei Arai, Rahul Bhatia, and Supriya Kapoor, editors, *Proceedings of the Future Technologies Conference (FTC) 2019*, pages 578–589, Cham, 2020. Springer International Publishing.

- [77] J. MacQueen. Some methods for classification and analysis of multivariate observations. 1967.
- [78] Jonathan Feinberg, Vinzenz Gregor Eck, and Hans Petter Langtangen. Multivariate polynomial chaos expansions with dependent variables. *SIAM Journal on Scientific Computing*, 40(1):A199–A223, 2018.
- [79] John D Jakeman, Fabian Franzelin, Akil Narayan, Michael Eldred, and Dirk Plfuger. Polynomial chaos expansions for dependent random variables. *Computer Methods in Applied Mechanics and Engineering*, 351:643–666, 2019.
- [80] Sharif Rahman. A polynomial chaos expansion in dependent random variables. *Journal of Mathematical Analysis and Applications*, 464(1):749–775, 2018.
- [81] Adam Bobrowski. *Functional analysis for probability and stochastic processes: an introduction*. Cambridge University Press, 2005.
- [82] Dongbin Xiu and George Em Karniadakis. The Wiener-Askey polynomial chaos for stochastic differential equations. *SIAM Journal on Scientific Computing*, 24(2):619–644, 2002.
- [83] Xiaoliang Wan and George Em Karniadakis. Multi-element generalized polynomial chaos for arbitrary probability measures. *SIAM Journal on Scientific Computing*, 28(3):901–928, 2006.
- [84] Christian Soize and Roger Ghanem. Physical systems with random uncertainties: chaos representations with arbitrary probability measure. *SIAM Journal on Scientific Computing*, 26(2):395–410, 2004.
- [85] John D Jakeman, Michael S Eldred, and Khachik Sargsyan. Enhancing l1-minimization estimates of polynomial chaos expansions using basis selection. *Journal of Computational Physics*, 289:18–34, 2015.

- [86] Jerrad Hampton and Alireza Doostan. Basis adaptive sample efficient polynomial chaos (base-pc). *Journal of Computational Physics*, 371:20–49, 2018.
- [87] Wanxin He, Yan Zeng, and Gang Li. An adaptive polynomial chaos expansion for high-dimensional reliability analysis. *Structural and Multidisciplinary Optimization*, 62(4):2051–2067, 2020.
- [88] Paul Diaz, Alireza Doostan, and Jerrad Hampton. Sparse polynomial chaos expansions via compressed sensing and d-optimal design. *Computer Methods in Applied Mechanics and Engineering*, 336:640–666, 2018.
- [89] Paul G Constantine, Michael S Eldred, and Eric T Phipps. Sparse pseudospectral approximation method. *Computer Methods in Applied Mechanics and Engineering*, 229:1–12, 2012.
- [90] Patrick R Conrad and Youssef M Marzouk. Adaptive smolyak pseudospectral approximations. *SIAM Journal on Scientific Computing*, 35(6):A2643–A2670, 2013.
- [91] Justin Winokur, Daesang Kim, Fabrizio Bisetti, Olivier P Le Maître, and Omar M Knio. Sparse pseudo spectral projection methods with directional adaptation for uncertainty quantification. *Journal of Scientific Computing*, 68(2):596–623, 2016.
- [92] Gregery T Buzzard. Efficient basis change for sparse-grid interpolating polynomials with application to t-cell sensitivity analysis. *Computational Biology Journal*, 2013, 2013.
- [93] Dimitrios Loukrezis and Herbert De Gersen. Adaptive sparse polynomial chaos expansions via leja interpolation. *arXiv preprint arXiv:1911.08312*, 2019.
- [94] Alireza Doostan and Houman Owhadi. A non-adapted sparse approximation of pdes with stochastic inputs. *Journal of Computational Physics*, 230(8):3015–3034, 2011.
- [95] Panagiotis Tsilifis, Xun Huan, Cosmin Safta, Khachik Sargsyan, Guilhem Lacaze, Joseph C Oefelein, Habib N Najm, and Roger G Ghanem. Compressive sensing adap-

tation for polynomial chaos expansions. *Journal of Computational Physics*, 380:29–47, 2019.

- [96] Ryan M Rifkin and Ross A Lippert. Notes on regularized least squares. 2007.
- [97] Xuerong Mao, Sotirios Sabanis, and Eric Renshaw. Asymptotic behaviour of the stochastic Lotka–Volterra model. *Journal of Mathematical Analysis and Applications*, 287(1):141–156, 2003.
- [98] Dale E Seborg, Thomas F Edgar, Duncan A Mellichamp, and Francis J Doyle III. *Process dynamics and control*. John Wiley & Sons, 2016.
- [99] Francesca Chillà and Joerg Schumacher. New perspectives in turbulent rayleigh–bénard convection. *The European Physical Journal E*, 35:1–25, 2012.

Appendix A. Projection onto the tangent space

In the neighborhood of $\mathbf{X}_1 \in \mathcal{G}_{p,n}$, a point \mathbf{X}_2 can be mapped onto the tangent plane $\mathcal{T}_{\mathbf{X}_1}$ using the logarithmic mapping $\log_{\mathbf{X}_1}(\mathbf{X}_2) = \mathbf{\Gamma}$. The inverse mapping onto the manifold can be performed using the exponential mapping $\exp_{\mathbf{X}_1}(\mathbf{\Gamma}) = \mathbf{X}_2$ which is derived by taking the thin SVD of $\mathbf{\Gamma}_1$, $\mathbf{\Gamma}_1 = \mathbf{U}\mathbf{\Sigma}\mathbf{V}^\top$, i.e.

$$\mathbf{X}_2 = \exp_{\mathbf{X}_1}(\mathbf{U}\mathbf{\Sigma}\mathbf{V}^\top) = \mathbf{X}_1\mathbf{V}\cos(\mathbf{\Sigma})\mathbf{Q}^\top + \mathbf{U}\sin(\mathbf{\Sigma})\mathbf{Q}^\top. \quad (\text{A.1})$$

where \mathbf{U} and \mathbf{V} are orthonormal matrices, $\mathbf{\Sigma}$ is diagonal matrix with positive real entries, and \mathbf{Q} is an orthogonal $n \times n$ matrix. Requiring that $\mathbf{\Gamma}$ lies on $\mathcal{T}_{\mathbf{X}_1}$, defines the following set of equations

$$\mathbf{V}\cos(\mathbf{\Sigma})\mathbf{Q}^\top = \mathbf{X}_1^\top\mathbf{X}_2. \quad (\text{A.2a})$$

$$\mathbf{U}\sin(\mathbf{\Sigma})\mathbf{Q}^\top = \mathbf{X}_2 - \mathbf{X}_1\mathbf{X}_1^\top\mathbf{X}_2. \quad (\text{A.2b})$$

Multiplying (A.2a) by the inverse of (A.2b) yields

$$\mathbf{U}\tan(\mathbf{\Sigma})\mathbf{V}^\top = (\mathbf{X}_2 - \mathbf{X}_1\mathbf{X}_1^\top\mathbf{X}_2)(\mathbf{X}_1^\top\mathbf{X}_2)^{-1}. \quad (\text{A.3})$$

The exponential mapping can be performed by taking the thin SVD of the matrix $\mathbf{M} = (\mathbf{X}_2 - \mathbf{X}_1 \mathbf{X}_1^\top \mathbf{X}_2)(\mathbf{X}_1^\top \mathbf{X}_2)^{-1} = \mathbf{U} \mathbf{\Sigma} \mathbf{V}^\top$. The logarithmic map can be defined by inversion of Eq. (A.3) as [71]:

$$\log_{\mathbf{X}_1}(\mathbf{X}_2) = \mathbf{\Gamma} = \mathbf{U} \tan^{-1}(\mathbf{\Sigma}) \mathbf{V}^\top. \quad (\text{A.4})$$

Appendix B. Steps of the proposed methodology

A summary of the steps is given below.

Algorithm 3

Require: A dataset $\{\boldsymbol{\theta}_i, \mathbf{y}_i\}_{i=1}^{\mathcal{N}}$

Project \mathbf{y}_i on the Grassmann: $\mathbf{y}_i = \mathbf{U}_i \mathbf{\Sigma}_i \mathbf{V}_i^\top$

Perform Riemannian K-means on $\{\mathbf{U}_i\}_{i=1}^{\mathcal{N}}$ on the Grassmann using Algorithm 2

For each cluster C_h perform Principal Component Analysis using Algorithm 1:

- Find the Karcher means of points \mathbf{U}_j and $\mathbf{V}_j \in C_h$ using Eq.(1)
- Project the points $\mathbf{U}_j/\mathbf{V}_j$ onto the tangent spaces with origin the corresponding Karcher means using the logarithmic mapping (see Appendix A)
- On each tangent space perform Principal Component Analysis

For each cluster C_h train three PCE surrogates according to Eq.(22).

For a new realization in the parameter space $\boldsymbol{\theta}^*$:

- Find the nearest neighbour of $\boldsymbol{\theta}^*$ in the parameter space using Eq.(23)
 - Use the corresponding trained PCE to predict:
 - the tangent vectors according to Eqs.(24a) and (24b)
 - the singular values $\mathbf{\Sigma}_j$ according to Eq.(26)
 - Map the predicted tangent vectors onto the Grassmannian with the exponential mapping (see Appendix A)
 - Invert the SVD to predict the full-field solution according to Eq.(27)
-